University of Nevada, Reno

Joint Optimization of Vertical Component Gravity and Seismic P-wave First Arrivals by Simulated Annealing

A thesis submitted in partial fulfillment of the
requirements for the degree of
Master of Science in Geophysics

by

Kyle J. Basler-Reeder

Dr. John N. Louie, Thesis Advisor

May, 2015

UNIVERSITY OF NEVADA, RENO

THE GRADUATE SCHOOL

We recommend that the thesis

prepared under our supervision by

Kyle J. Basler-Reeder

entitled

Joint Optimization of Vertical Component Gravity and Seismic P-wave First Arrivals by Simulated Annealing

be accepted in partial fulfillment of the

requirements for the degree of

MASTER OF SCIENCE

John N. Louie, Ph.D., Advisor

Graham Kent, Ph.D., Committee Member

Satish Pullammanappallil, Ph.D., Committee Member

Pavel Solin, Ph.D., Graduate School Representative

David W. Zeh, Ph.D., Dean, Graduate School

May, 2015

Abstract

Joint Optimization of Vertical Component Gravity and Seismic P-wave First Arrivals by Simulated Annealing

Kyle Basler-Reeder[1]

John Louie[1]

Satish Pullammanappallil[1,2]

Graham Kent[1]

[1] Nevada Seismological Laboratory, University of Nevada, Reno, NV

[2] Optim, Reno, NV

Simultaneous joint seismic-gravity optimization improves P-wave velocity models in areas with sharp lateral velocity contrasts. Optimization is achieved using simulated annealing, a metaheuristic global optimization algorithm that does not require an accurate initial model. Balancing the seismic-gravity objective function is accomplished by a novel approach based on analysis of Pareto charts. Gravity modeling uses a newly developed convolution model, while seismic modeling utilizes the highly efficient Vidale eikonal equation traveltime generation technique. Synthetic tests show that joint optimization improves velocity model accuracy and provides velocity control below the deepest headwave raypath. Restricted offset range migration analysis provides insights into both pre-critical and gradient reflections in the dataset.

Detailed first arrival picking followed by trial velocity modeling remediates inconsistent data. We use a set of highly refined first arrival picks to compare results of a

convergent joint seismic-gravity optimization to the Plotrefa™ and SeisOpt® Pro™ velocity modeling softwares. Plotrefa™ uses a nonlinear least squares approach that is initial model dependent and produces shallow velocity artifacts. SeisOpt® Pro™ utilizes the simulated annealing algorithm, also produces shallow velocity artifacts, and is limited to depths above the deepest raypath. Joint optimization increases the depth of constrained velocities, improving reflector coherency at depth. Kirchoff prestack depth migrations reveal that joint optimization ameliorates shallow velocity artifacts.

Seismic and gravity data from the San Emidio Geothermal field of the northwest Basin and Range province demonstrate that joint optimization changes interpretation outcomes. The prior shallow valley interpretation gives way to a deep valley model, while shallow antiformal reflectors that could have been interpreted as antiformal folds are flattened. Furthermore, joint optimization provides a more clear picture of the rangefront fault. This technique can readily be applied to existing datasets and could replace the existing strategy of forward modeling to match gravity data.

One's mind, once stretched by a new idea, never regains its original dimensions.

Oliver Wendell Holmes Sr.

Acknowledgements

None of this work would have been possible without the financial support of the Optim fellowship provided to me by Dr. Satish Pullammanappallil and Bill Honjas of Optim. I am personally inspired by their philanthropy and greatly appreciative of the many fruitful discussions I had with Dr. Pullammanappallil in advancing this work. Southern California Edison also provided financial support. I also thank the Nevada Seismological Laboratory for providing me with so many opportunities to develop my talent as an exploration geophysicist.

The San Emidio geothermal field was researched thoroughly before I started my thesis. I would like to acknowledge Greg Rhodes for his 2011 thesis, *Structural Controls of the San Emidio Geothermal System, Northwestern Nevada*, which rapidly brought me up to speed on the geologic setting and prior geophysical work. Gravity forward modeling results by Bill Teplow of U.S. Geothermal were very useful for model calibration. I highly regard the U.S. Department of Energy's choice to allocate funds from the American Recovery and Reinvestment Act towards creating a powerful geophysics dataset at a geothermal site. Those funds not only helped U.S. Geothermal, but also made my research project possible, and ultimately led me to a career in the oil industry. I thank U.S. Geothermal for granting permission to use the seismic and gravity data acquired at their San Emidio geothermal field.

I benefitted from discussions with many professors. My advisor, Dr. John Louie, inspired me to innovate from day one and opened my eyes to new ways of thinking. Throughout this research, I used a variety of Dr. Louie's C codes and his open-source software package, Viewmat for Java (http://crack.seismo.unr.edu/jrg/). Dr.

Graham Kent continuously raised the bar and granted access to once in a lifetime opportunities, including a 3-week marine seismic survey. Dr. Kent provided support with the seismic processing package SIOSEIS, which I used for data visualization and to perform surgical muting (http://sioseis.ucsd.edu). Dr. Steve Wesnousky taught me the importance of communicating observations effectively as a scientist and his masterpieces on the Walker Lane originally got me interested in attending UNR. Dr. Ken Smith answered all of my questions about earthquakes in Nevada and gave me helpful writing tips. Dr. John Anderson helped me understand singular value decomposition and gravity modeling. Dr. Glenn Biasi reminded me of the power of the outmoded combination of paper and pencil. Dr. Wendy Calvin, a fellow Coloradan, sold me on living in Reno with the promise of a mild climate; I am pleased to report that she was correct. I would also like to thank Dr. Jim Faulds for taking time to discuss my structural interpretations.

Behind the scenes of every great organization is an excellent administrative staff. I would like to acknowledge Erik Williams, who always knew the right answers regarding travel forms; Lori McClelland, who taught me how to use the fax machine a dozen times; Marie Russell, who gave me access to register for courses; and Melodie Gander, for readily providing me with the keys to Mackay vehicles.

Making it through graduate school was made easier by the peers I came to know, such as Joe Dierkhising, who was the first friend I made and my greatest ally in understanding the works of Jon Claerbout; Christine Ruhl, who assisted me greatly with my GMT map and whose talent as a programmer was inspiring; Tyler Seaman, who completed Team Petro; Steve Angster, an officemate whose geological insights proved invaluable; Annie Kell, my partner in resolving the many nuances of LaTeX;

Jayne Bormann for crucial help with Matlab; Paul Schwering, who introduced me to the gravimeter and magnetometer; Kyle Gray, who refreshed my knowledge of Oasis Montaj and organized a critical trip for us to a geophysics symposium; Andrew Sadowski, for discussions about the regional tectonic history at San Emidio; Ryan Anderson, for helping me obtain elusive GRC papers; Dustin Naphan, who assisted me in the field during my first gravity survey; and Matt Folsom, for interesting discussions and offering to host my graduation party.

Other persons of note who helped along the way are Dr. Leif Cox of the University of Utah about implementing Green's tensors; Jan Simon of Heidelberg University, for masterful Matlab explanations; Gabe Plank, who helped me make the switch to C coding in Xcode; Mark Williams for C coding tips and advice on making it through graduate school; John Torrisi for being thoughtful and providing me with a satellite phone when I ventured far into the desert; Dr. Dennis Harry of Colorado State University for discussions here and there; and Dr. Kaleb Scarberry of the USGS for his perspective on graduate education. Thanks go out to everyone at ExxonMobil for facilitating an incredible summer internship. Most of all, thanks go to my family, who unwaveringly supported me all the way through.

Contents

List of Figures

Chapter 1 Introduction

The research efforts outlined in this thesis were a collaborative effort between the Nevada Seismological Laboratory at the University of Nevada, Reno and Optim. The driving force behind our work is a desire to improve seismic imaging for geothermal resources, which in turn could result in higher geothermal exploration drilling success rates (Faulds et al., 2010; Louie et al., 2012; Harris, 2012). Louie et al. (2012) shows that strides have been made towards solving the velocity modeling problems inherent to seismic imaging in the complex geologic setting of the Great Basin, but there is still room for improvement.

This thesis utilizes high quality seismic and gravity datasets collected by Optim and MWH Geo-Surveys for a U.S. Geothermal exploration project funded by the U.S. Department of Energy's American Recovery and Reinvestment Act (ARRA). The project's objective was to synthesize structural geology and exploration geophysics to delineate subsurface fault intersections at a known geothermal system. These fracture systems make desirable drilling targets for power production facilities, as they are generally permeable conduits for high temperature fluids (Faulds et al., 2006). Other UNR student theses based on geothermal exploration projects funded through ARRA include, but are not limited to: Drakos (2007), Delwiche (2007), Vice (2008), Anderson (2013), and Mayhew (2013).

Drakos (2007) concluded that northern Basin and Range normal faults are kinematically linked to major dextral faults of the northern Walker Lane, such as the Pyramid Lake fault. Drakos (2007) also found that a ˜1 km thick Miocene volcanic section rests disconformably on thin Oligocene ash-flow tuffs, which unconformably overlies Mesozoic granitic, metasedimentary, and metavolcanic basement. Drakos (2007) states that the Miocene and Oligocene volcanic sections have concordant eastward-dipping foliations of ˜20°, suggesting the Pyramid Lake region did not experience east-west extension prior to ˜13 Ma. Delwiche (2007) found that paleoval-

leys in the Pah Rah Range, which is south of Pyramid Lake, trended ˜265° to ˜280°. Delwiche (2007) also reports ˜25° to ˜40° clockwise rotations in eastern Warm Springs Valley. Vice (2008) states that tufa towers at The Needles and Astor Pass are structurally controlled and suggests that tufa towers, fault intersections, and dilational fault tendency are good indicators of potential blind geothermal systems. Anderson (2013) also found Miocene and Oligocene volcanic and sedimentary rocks overlying Mesozoic basement. Anderson (2013) concluded that Astor Pass is controlled by a west-northwest-trending least principal stress in a normal faulting regime and stresses the importance of paying attention to regional structural patterns. Mayhew (2013) points out that hydrologic studies indicate that the Tertiary Pyramid sequence is too permeable and transmissive to support discrete fault-fluid conduits, but this is not true for the Mesozoic basement.

Optim collected and processed ten lines of seismic data at San Emidio in 2010. The survey leveraged Vibroseis sources, advanced recording equipment, and large maximum offsets to produce a very high quality seismic dataset. Optim used their software, SeisOpt® Pro™, to create seismic velocity models using first arrival picks picked off shot records. SeisOpt® Pro™ uses the simulated annealing algorithm, a nonlinear metaheuristic optimization technique that converges to the global error minima through a Monte Carlo approach. In 2011, results of the seismic imaging efforts were presented in Greg Rhode's master's thesis titled, "*Structural Controls of the San Emidio Geothermal System, Northwestern Nevada.*" While geologic complexities made imaging very difficult, the project was remarkably successful in demonstrating the effectiveness of applying advanced seismic imaging techniques to geothermal resource characterization. I aim to improve imaging to facilitate a new series of interpretations.

I completed initial first arrival picks for line 6 using Viewmat for Java software (http://crack.seismo.unr.edu/jrg/). Optim used those picks to create a new velocity model through SeisOpt® Pro™. Using a custom Matlab script, I plotted computed first-arrival traveltimes, observations, and associated residuals beside wiggle-trace

shot records. Through detailed examination, I discovered and resolved inconsistent data and inaccurate picks.

MWH Geo-Surveys collected and processed vertical-component gravity data in 2008. Teplow et al. (2011) examined seismic and gravity data sequentially, with a subsurface density profile being forward modeled to match and support the results of the seismic velocity model. In this thesis, I explore the potential of incorporating gravity data in the seismic processing workflow at the velocity model building step. My hypothesis is that a velocity model conforming to both seismic and gravity observations will produce superior seismic imaging results in comparison to a velocity model that only takes advantage of seismic data. This is made possible through the utilization of the time-honored empirical velocity-density relationship derived by G. H. F. Gardner and L. W. Gardner in 1974.

The development of my joint seismic-gravity optimization code took place in the Mathworks Matlab® (version R2013a) environment. My gravity forward modeling code was built from scratch out of necessity and was chosen for oral presentation at the 2014 Society of Exploration Geophysicists Annual International Meeting (Reeder et al., 2014). Optim provided me with a proprietary traveltime modeling code.

My thesis required me to conceive, write, test, and implement a variety of Matlab scripts, Matlab functions, C codes, and Fortran codes. What follows is a brief description of the most essential codes.

Matlab Scripts

1. Reeder_Wiggle.m reads in a seismic shot gather in SEG-Y format, first arrival picks in Viewmat format, and calculated first arrival traveltimes in SeisOpt® Pro™ format. The ability of this script to plot calculated and observed first arrival picks directly on shot records in wiggle trace format was leveraged to evaluate my initial first arrival picks. Plotting residuals next to the shot records revealed areas of inconsistent data. Reeder_Wiggle.m also creates a histogram of traveltime residuals, a plot of offset vs. traveltime misfit, and computes χ^2 values.

2. Reeder_SEGY_Header.m reads in a SEG-Y file and outputs all relevant header information. This script also scans trace headers to produce plan and cross-sectional views of shot and receiver locations. These plots helped understand survey geometry and gave the surveyed geophone location precision value used in my χ^2 analysis. Reeder_SEGY_Header.m also computes the Nyquist frequency and Nyquist wavelength to help understand aliasing criteria.

3. Reeder_TT_Output.m reads in a binary floating point velocity model and shot/receiver locations. The script loops over shot locations, plotting isotime contour plots on the input velocity model. I used this script to troubleshoot calculated first arrival times and demonstrated that my vertical model extension technique was incorrectly pulling up deep velocities, resulting in first arrival times that were too early. This was resolved by using lateral model extension. This script was very handy for validating the robustness of my traveltime generator and also writes the traveltime planes used by the aargKMig.c migration code.

4. Reeder_DualOpt.m is my joint optimization, which reads in first arrival picks,

gravity data, and a parameter file. The script outputs plots of iteration vs. energy, a Pareto chart, iteration vs. temperature, iteration vs. acceptance rate, a traveltime plot, a gravity model plot, and velocity/density models. Modifying the code to reset the model at each temperature grants the ability to conduct a temperature study. Running this script and examining the trend of error reduction in the Pareto chart is essential for objective function calibration.

Matlab Functions

1. Reeder_Deepray.m has inputs of a velocity model and source/receiver locations. This function loops over source and receiver locations, creating traveltime planes. Summing traveltime planes and computing the minimum traveltime for each easting element determines the first arrival ray path for each shot. Looping over each source-receiver first arrival ray path plane and computing the deepest ray path gives a vector of the deepest first arrival ray path through the model. This is useful to understand the depth of first-arrival-based velocity modeling control.

2. Reeder_Topography.m reads in model space dimensions and source/receiver locations. The function grids source and receiver locations, emplacing null elements to the top of the model above each source and receiver location. The function also sets elements to a value of unity below the null elements. The model pertubation function applies element-wise multiplication to the array that this function outputs to preserve the topography of the model.

3. Reeder_Model_Perturber.m reads in a velocity model and min/max velocities. A randomly sized rectangle, with a randomly determined origin, is generated with a random velocity in the specified range. The rectangle then replaces the corresponding elements of the input model. In order to obtain a uniform sampling distribution, the origin must be locatable up to one model dimension outside of the model space. The random rectangle can breach topography, so

topography is reset using the output of Reeder_Topography.m. This function is an essential component of any Monte Carlo style optimization.

4. Reeder_Arrivals.m reads in a velocity model and source/receiver locations. This function calls on a MEX function, Vidale_TURBO.c, which is a converted C code containing the Vidale (1988) method for traveltime generation provided to me by Optim. Reeder_Arrivals.m returns generated first arrival times for each source-receiver pair, which are compared to observed first arrival time picks to create residuals.

5. Talwani_TURBO_init.m reads in model space dimensions, element dimensions, and a vector of gravity station easting locations. This function detects the number of null density elements at each easting location to determine the correct vertical position of gravity stations. Running this one time prior to the optimization generates a convolution vector used by the gravity model described below.

6. Talwani_TURBO.m reads in output from Talwani_TURBO_init.m and a density model. It uses a convolution method to produce a gravity model. For efficiency, the convolution takes place in the MEX function Talwani_TURBO.c. This function outputs a gravity model that can be compared to observations for residual generation.

7. RMS_Error.m reads in two vectors of equal length and returns the RMS error according to the following formula:

$$\sigma = \sqrt{\frac{\sum_{i=1}^{n_x}(x_i^{observed} - x_i^{calculated})^2}{n_x}} \tag{1.1}$$

I used this in my objective function during optimization.

Fortran Codes

1. Viewmat_to_Plotrefa.m reads in a first arrival pick file in Viewmat format. This

code converts the picks to the input format required by Geometrics® Plotrefa™, which was used to create velocity models by the nonlinear least squares method.

2. Viewmat_to_SeisOpt.m also reads in a first arrival pick file in Viewmat format. This code projects picks onto a plane before writing a pick file in the input format needed for SeisOpt® Pro™, which was used to create velocity models by the simulated annealing method.

These Fortran codes are hard-coded for San Emidio line 6 seismic lines and would need to be modified for use with other datasets.

Code Testing

Use of the aforementioned codes required thorough testing. This testing was predominantly done in the Matlab environment, which facilitates automated viewing of data. Output of C and Fortran codes was imported to Matlab.

Reeder_Wiggle.m effectively displays first arrival energy; this was accomplished by manually setting gains, mutes, and windowing. The histogram plotting function agrees with synthetic data. Other scientists at UNR utilized Reeder_SEGY_Header.m and reported that it produced correct results. Plots of shot and receiver locations were cross-checked with survey information. Reeder_TT_ Output.m produced accurate isotime contour results even when confronted with the most extreme horizontal and vertical velocity gradients.

Reeder_DualOpt.m was the focus of most of my attention. Testing included plots of acceptance rates, energy, cooling schedule, and seismic/gravity models. Furthermore, the Code Analyzer tool in Matlab revealed many potential improvements in efficiency; most of these improvements came from vectorization of 'for' loops. Reeder_Topography.m gave the correct results for a variety of synthetic models, including models that lack topography. Reeder_Deepray.m generally obtains the deepest

ray. However, sometimes there are two shortest-time paths. When this occurs, the shallower ray may be chosen, which can lead to inaccurate results. When this occurs, the deepest ray will show a vertical 'tear' on one or both of the edges. This could be resolved by checking for the presence of two second derivative minima and choosing the deeper one.

Originally, Reeder_Model_Perturber.m's model perturbation was restricted to the model space, which led to a non-uniform element hitcount. Allowing perturbation to extend outside the model dimensions resolves this issue; generated hitcount maps now show a truly uniform distribution. Reeder_Arrivals.m produces reasonable first arrival times. However, for models with topography and flat refractors, the code produces jagged arrivals. This is due to the discretized nature of topography, which was mostly relieved by smoothing first arrival times.

Talwani_TURBO_init.m was validated by comparing computed results to analytical results of buried dikes and buried slabs. Talwani_TURBO.m produces results that are comparable to the commercial software package GM-SYS. RMS_Error.m was validated with synthetic error models. Manual checks Viewmat_to_Plotrefa.m output show correctness. Viewmat_to_SeisOpt.m works as expected, shown by opening data in SeisOpt® Pro™ and comparing to initial observations.

The main body of this thesis is a paper that will be submitted to the journal *Geophysics*, which is published by the Society of Exploration Geophysicists of Tulsa, Oklahoma.

Chapter 2 Geophysics Paper

2.1 Introduction

2.1.1 Motivation

The United States of America is the world leader in geothermal energy extraction, with current electrical generation capacity of 3,442 MW and 124 developing projects (Matek, 2014). The majority of these new developments are in the state of Nevada, due to a combination of favorable business settings and a relatively thin crust that results in a high geothermal gradient (Blackwell et al., 2011). Matek (2014) states that only 40% of total geothermal production potential has thus far been realized in Nevada. Coolbaugh et al. (2006) estimate that half of the remaining potential resides in reservoirs with no obvious surface expression, which are commonly referred to as 'blind' systems (Cumming, 2009). Blind systems tend to occur in areas of high fracture density, which produces high permeability (Colwell et al., 2012; Dering, 2013; Jolie et al., 2015; Anderson, 2013; Kent, 2013; Mayhew, 2013; Vice, 2008). Faulds et al. (2006) conducted a regional study and found that there is a high probability of finding geothermal systems at fault intersections. Louie et al. (2012) point out that due to resolution and depth of investigation constraints, seismic reflection imaging is the only geophysical method capable of precisely imaging fault intersections at production depths. The high cost of exploratory drilling campaigns and low success rates hamper new development, which can be remedied by geophysical investigation (Faulds et al., 2010; Louie et al., 2012; Harris, 2012).

2.1.2 Geologic Setting

One example of an active geothermal power plant where geophysical investigation has been applied is San Emidio, which is operated by U.S. Geothermal and is located roughly 100 km (60 miles) NNE of Reno, Nevada (Figure 2.1). San Emidio is situ-

ated just east of the transtensional Walker Lane in the extensional northern Basin and Range province. Rhodes (2012) describes the geothermal reservoir as being found in a right-stepping series of hard-linked, north-striking, west-dipping normal faults along the western flank of the northern Lake Range. Installed energy production capacity of 12.75 MWe is derived from a thermal anomaly at 520 m (1,700 ft) depth, with estimated total resource potential of 44 MWe (Rhodes, 2012; Matek, 2014)). Eneva et al. (2011) discuss surficial temperature and subsidence anomalies that extend northward from the current production area, which suggests the possibility of another geothermal reservoir in the northern exploration area. In order to help guide exploratory drilling, Optim collected seismic and gravity data at San Emidio through a U.S. Dept. of Energy American Recovery and Reinvestment Act project. Teplow et al. (2011) states that the project's objective was to test the feasibility of utilizing geophysical techniques to identify large-aperture fractures at depth.

2.1.3 Objective

Sharp density and seismic velocity gradients are created by depositional and fault contacts of unlithified valley fill adjacent to crystalline bedrock (e.g., Abbott et al. (2001)). This complex structure produces rapid lateral velocity variations that preclude the use of standard seismic analysis routines used in sedimentary systems (Louie et al., 1988; Honjas and Pullammanappallil, 1997; Louie et al., 2012). Increased subsurface complexity demands more advanced migration algorithms, as well as increased velocity model accuracy. I utilize Kirchhoff prestack depth migration (KPSDM), which is able to handle structure with any range of dip, and is regarded as robust in the presence of complex velocity variations (Louie and Qin, 1991; Biondi et al., 2014). KPSDM is based on the Born, WKBJ, and far-field assumptions (Louie et al., 1988). As with any migration algorithm, using an accurate velocity model is essential, with particular importance on lateral velocity variations (Louie and Qin, 1991; Tieman, 1995; Luo and Hale, 2014). This is due to the way that KPSDM deforms short-wavelength reflectors around the long-wavelength velocity model. Pullammanappallil

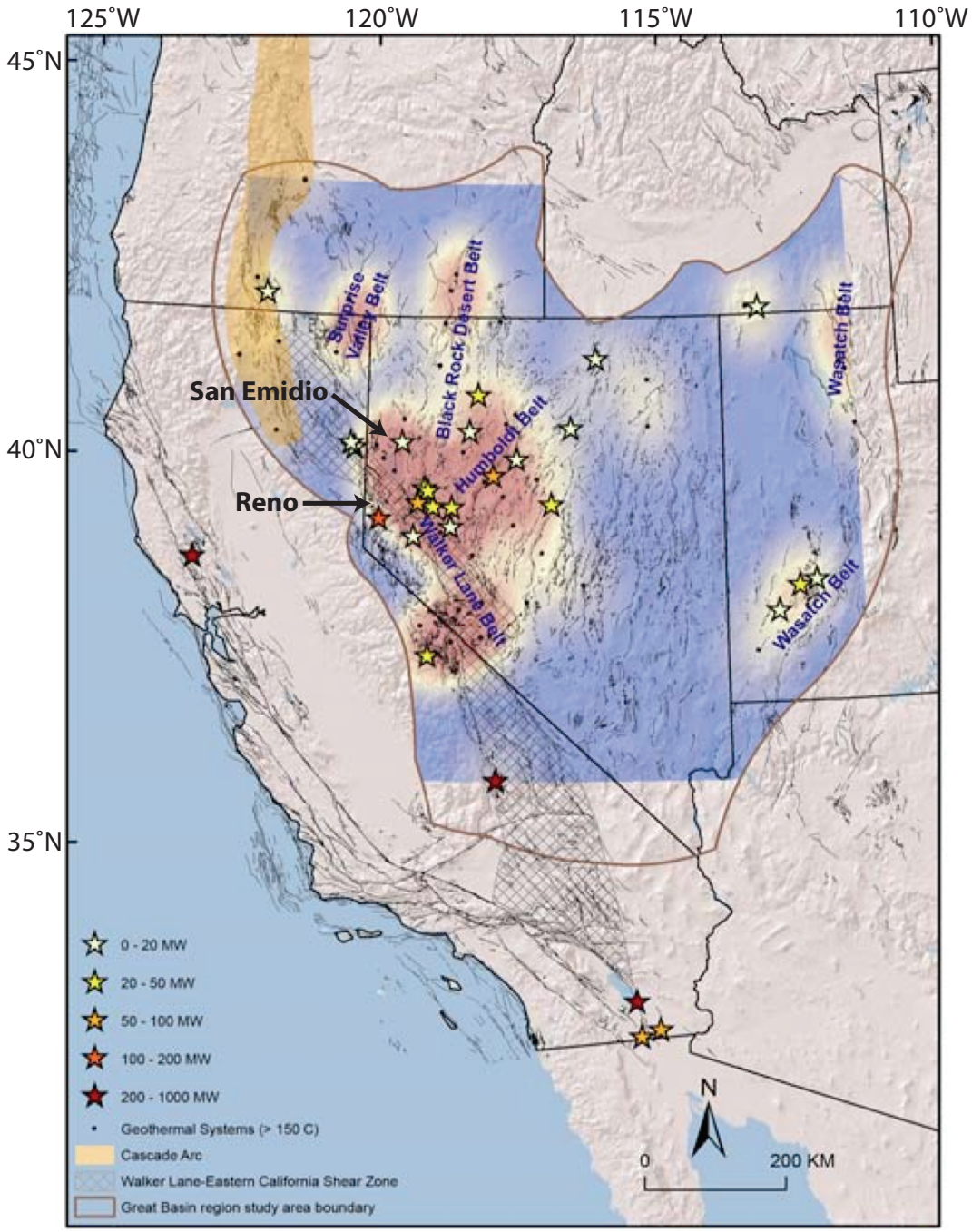

Figure 2.1: Regional map of the western United States shaded for density of high-temperature (<150° C) geothermal systems; warm colors indicate higher density. The drainage divide of the Great Basin is delineated with a brown line. The area of the Walker Lane, a zone of dextral transtension, is shown by a diagonal hatched pattern. San Emidio is located just east of the Walker Lane in the northern Basin and Range. Stars indicate active geothermal power plants. Modified from Faulds et al. (2012).

(1994) introduced seismic velocity optimization using the simulated annealing algorithm (SA), which has proven success at sites with strong lateral velocity contrasts. Louie et al. (2012) discusses how the paired use of KPSDM and seismic SA has solved many of the problems inherent to imaging geothermal sites.

Optim produced a San Emidio line 6 velocity model using seismic SA (Teplow et al., 2011). Converting the preexisting line 6 velocity model to a density model using the empirical velocity-to-density relationship of (Gardner et al., 1974) followed by gravity modeling reveals a noticeable misfit; this suggests that including gravity in the velocity model building step would result in a different outcome. SA shows ambiguity at depths below the lowest raypath, but gravity does not share this limitation (Pullammanappallil, 1994). Vasco et al. (1996) show there can be many equivalent-error solutions in velocity optimization, which limits resolvability of complex structure and sharp velocity gradients. Typically, gravity models are manually created to support seismic velocity models (e.g., O'Donnell Jr et al. (2001)). Including gravity constraints into the velocity-building step is one means of increasing the depth of constrained velocities and reducing nonuniqueness.

Joint seismic-gravity optimization is the most successful and well-studied technique that incorporates two geophysical datasets to arrive at one solution, and models produced by the simultaneous optimization of multiple datasets are often more geologically realistic than models constrained by a single type of data (Roy et al., 2005). Rovetta et al. (2013) demonstrate that joint seismic-gravity optimization improves seismic imaging in areas with rapid lateral velocity variation. San Emidio is a prime location to test joint seismic-gravity optimization, not only because of untapped resource potential and an outstanding dataset, but also due to a sharp density and velocity contrast at the alluvium-bedrock contact. However, joint optimization using the SA algorithm is a surmountable goal, as it is often difficult to get models to converge. Difficulties stem from the choice of an objective function that balances seismic and gravity constraints and the determination of an effective cooling schedule (Basu and Frazer, 1990; Sen and Stoffa, 2013).

My hypothesis is that obtaining a stable joint optimization algorithm will lead to more accurate seismic velocity models. These improved velocity models could increase interpretability of migrations by enhancing the resolvability of structure at depth through increased coherency of deep reflectors. This outcome could positively impact geothermal drilling success rates in the Great Basin.

2.2 Data and Methods

2.2.1 Seismic and Gravity Data Processing

Optim collected ten seismic lines at San Emidio (Figure 2.2). Line 6 is focused on for its proximity to the geothermal production zone. Shot records for line 6 have a maximum offset of 3,220 m (10,600 ft) and a receiver spacing of 17 m (55 ft). Optim stacked ten 8-100 Hz Vibroseis sweeps at each shot point, followed by cross-correlation with the source sweep as described in Cambois (2000). I made nearly 10,000 first arrival picks on raw, unfiltered records (Figure 2.3), followed by trial velocity modeling using the seismic SA optimization of SeisOpt® Pro™. I made first arrival picks in the center peak of the Klauder wavelet that results from Vibroseis source correlation. Careful inspection of plotted calculated and observed traveltimes on AGC-gained wiggle trace shot records with interior and exterior muting revealed areas where I picked inconsistent data, such as shallow diffractions, pre-arrival sweep correlation artifacts, and shot-to-shot cycle skipping. Removal of picks in problem areas reduced the number of picks by 30%, greatly reducing the amount of inconsistent data; χ^2 values for the initial and final runs are 2.3 and 0.97, respectively. Obtaining a χ^2 value of 2.3 indicates the data are underfit, while a value 0.97 implies a very slight overfit (Van Avendonk et al., 2001). Empirically determined migration processing parameters are based on the effectiveness of suppressing surface/air wave amplitudes, while preserving fault reflections (Figure 2.4).

Gravity data consist of 726 vertical component gravity measurements (Figure 2.2). Gravity station selection is based on proximity to seismic line 6, resulting in 16 equidis-

tant data points with a spacing of 205 m (672 ft). Three extra stations on the western side are provided by linear interpolation of nearest points. MWH Geo-Surveys applied drift and tidal corrections, which are on the order of 0.2 mGal; this is two orders of magnitude smaller than the range of gravity measurements, and is therefore negligible. MWH Geo-Surveys determined terrain and elevation corrections in the field. Due to the way that my optimization automatically handles topographic corrections on smaller scales, inner ring corrections are not needed. When conducting a gravity survey, precise topographic measurements are critical to proper gravitational modeling; an error of 1 m in vertical elevation can result in a change of 0.3 mGal (Telford and Sheriff, 1990). I used elevation data from SEG-Y trace headers with a precision of 1 foot (0.3 m). Gravity stations are not located directly on the seismic line, but relative elevation changes are preserved; these errors are assumed to be within measurement error. MWH Geo-Surveys applied Bouguer corrections using a density of 2.5 g/cc, which is close to measured basement densities in this region (Drakos, 2007; Mankhemthong, 2008).

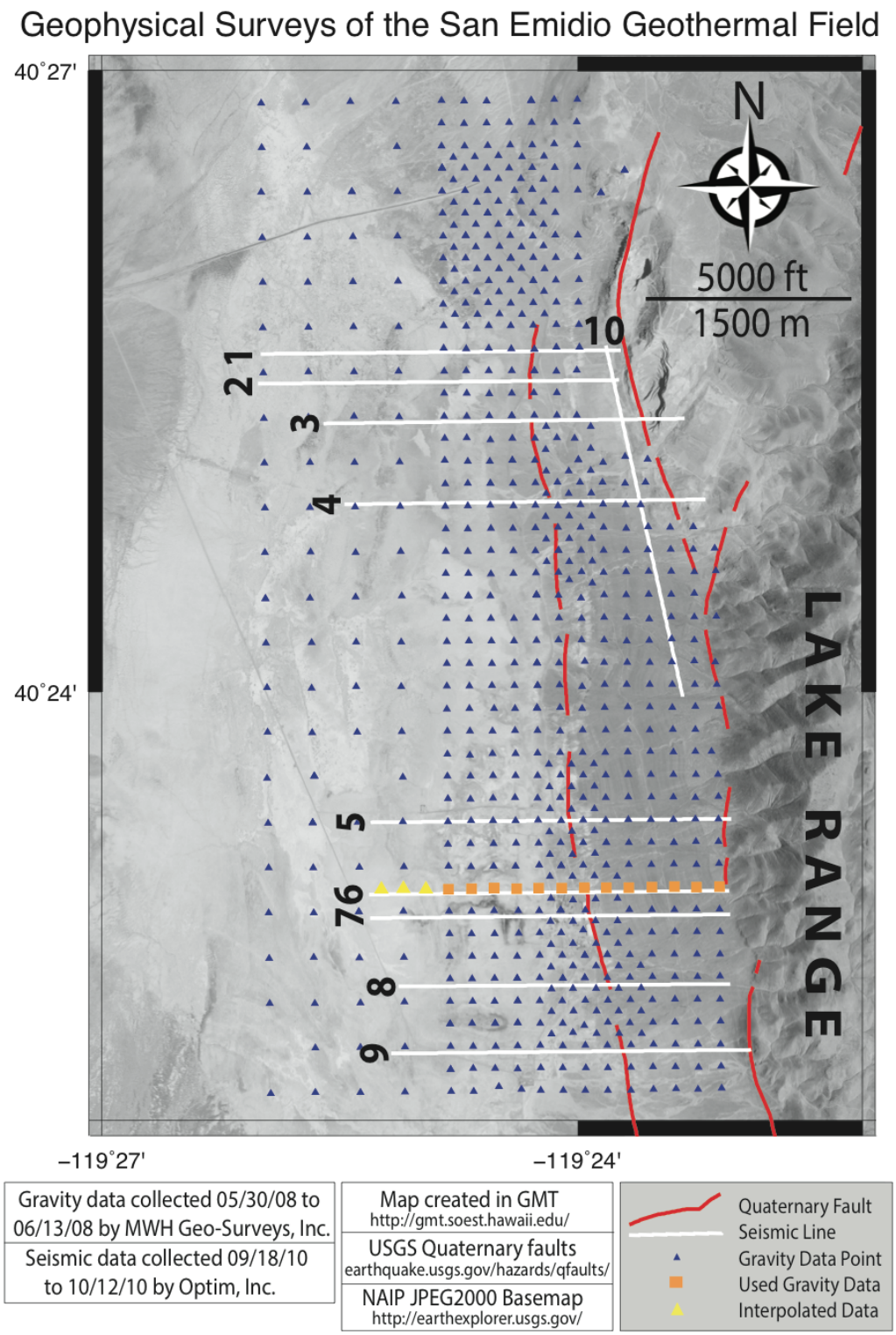

Figure 2.2: Overview of geophysical data collected at San Emidio. Quaternary faults are indicated by red lines. White lines show the extent of seismic surveys. Blue triangles show the positions of all gravity data points. Utilized gravity measurements are indicated by orange squares and yellow triangles.

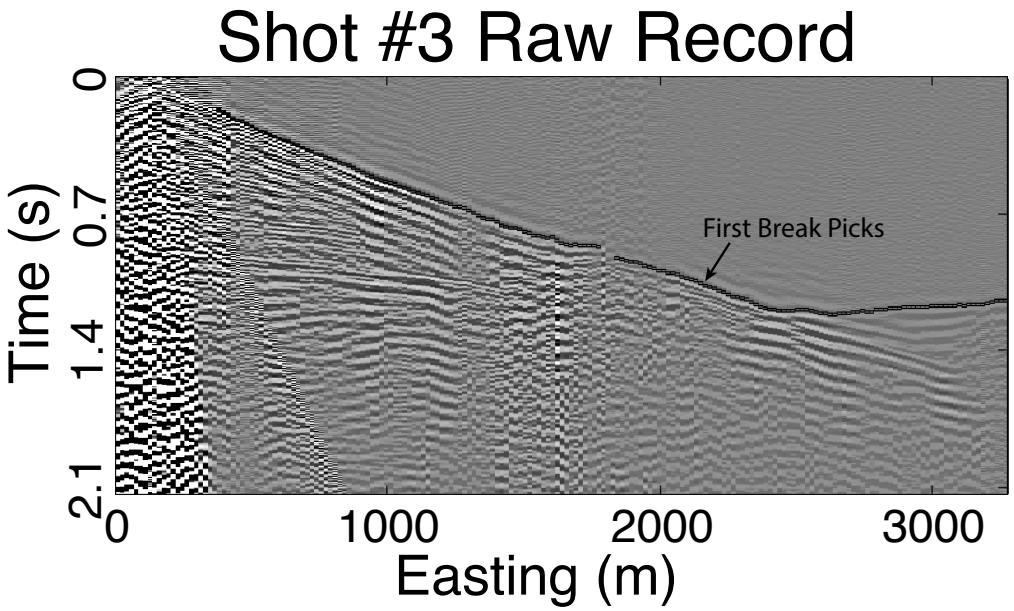

Figure 2.3: First 2.1 seconds of a shot record with amplitude clipped at 2*RMS. First arrival picks are indicated by black rectangles.

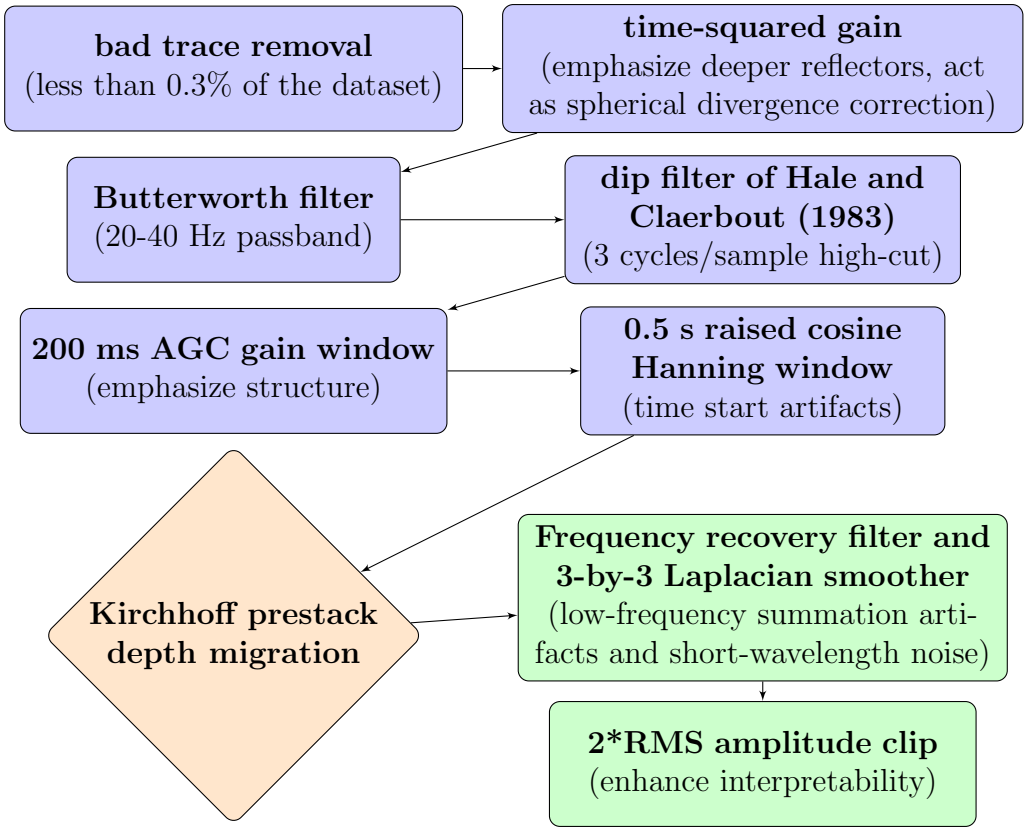

Figure 2.4: Migration pre-processing (blue) and post-processing (green) flows.

2.2.2 Plotrefa™ Velocity Modeling

Plotrefa™ by Geometrics® creates velocity models using a least squares technique (Figure 2.9). The software updates raypaths after each iteration, which makes it non-linear. Plotrefa™ uses a deterministic traveltime algorithm and iteratively updates velocity models using an approximated tomographic back projection (Geometrics, 2009). Due to the fact that Plotrefa™ only accepts new models with lower error, it is initial model dependent and classified as a local search algorithm. The initial model has 90 discretized horizontal layers, with velocity increasing linearly from 1,500 m/s (4,900 ft/s) at the surface to 6,500 m/s (21,000 ft/s) at a depth of 1,500 m (4,950 ft); tests with alternate initial models revealed that this range results in the lowest final RMS error of 13 ms.

2.2.3 SeisOpt® Pro™ Velocity Modeling

Optim's SeisOpt® Pro™ produces velocity models by seismic SA optimization (Figure 2.11). Similar to Plotrefa™, the package also uses deterministic traveltime calculations, but differs by updating models using a Monte Carlo approach. The seismic SA algorithm of SeisOpt® Pro™ does not require an accurate initial model (Pullammanappallil, 1994). When optimization commences, SeisOpt® Pro™ initially explores the entire solution space. Across many iterations, the SA algorithm switches to a local optimization to begin exploiting a narrow region. Due to the fact that the velocity model only returns values above the deepest raypath, model extension populates the rest of my rectangular model space. Generating isotime contour plots tests the validity of model extension. Extension by downward linear interpolation from velocity elements along the deepest raypath to the laterally translated deepest velocity element of the model creates a concave bedrock profile, resulting in generated traveltimes arriving too early. In order to rectify this issue, a manual and ad hoc lateral extension strategy produces a velocity model with a flat bedrock interface extending west towards the valley axis.

2.2.4 Velocity to Density Conversion

My joint optimization scheme is predicated upon observations that density tends to be nonlinearly proportional to seismic velocity. Brocher (2005) provides an excellent overview of various empirical velocity-density relationships to choose from (Figure 2.5). Ludwig et al. (1970) produced the Nafe-Drake curve, which is valid for all rock types with a v_p range of 1.5 km/s to 8.5 km/s. Gardner et al. (1974) derived the most widely used equation, which is valid for sedimentary rocks with v_p from 1.5 km/s to 6.1 km/s. Christensen and Mooney (1995) and Godfrey et al. (1997) provide linear relationships for crystalline rocks at 10 km depth, with v_p ranges of 5.5 km/s to 7.5 km/s and 5.9 km/s to 7.1 km/s, respectively. The Gardner relationship provides the most reasonable densities when extrapolated to velocities below 1.5 km/s; the minimum velocity for my optimization is 500 m/s.

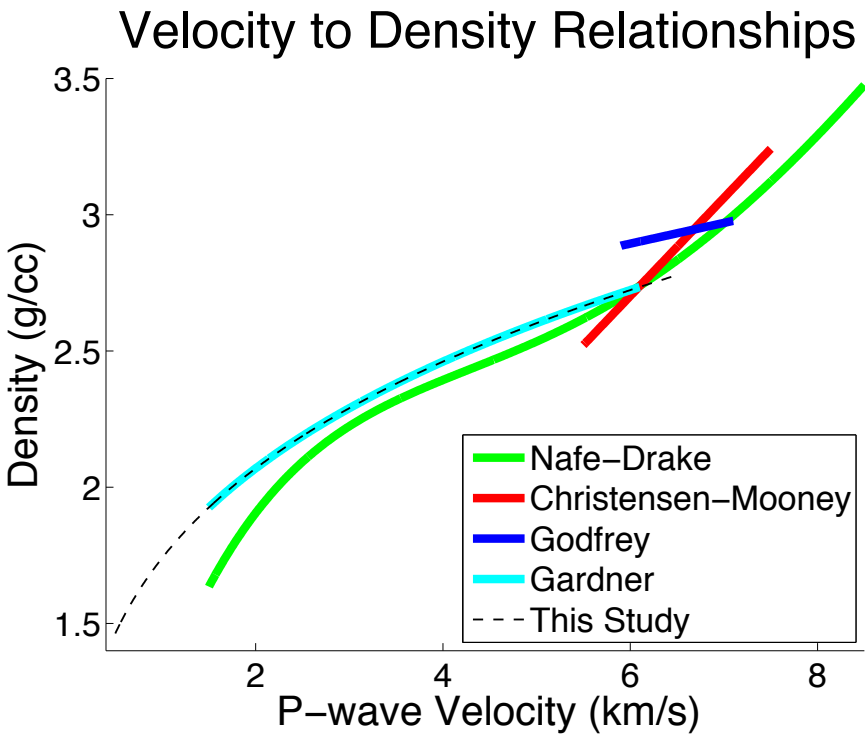

Figure 2.5: Velocity-to-density relationships. The Nafe-Drake relationship is indicated by a green line; Christensen-Mooney by a red line; Godfrey by a blue line; and Gardner by a teal line. The extrapolated Gardner relationship used in this study is shown by a dashed black line.

2.2.5 Forward Modeling Algorithms

Sen and Stoffa (2013) posit that fully understanding the limitations and assumptions inherent to forward modeling is the most important step in developing a successful optimization algorithm. Monte Carlo optimizations can require hundreds of thousands of iterations, necessitating the use of an efficient forward modeling scheme. Furthermore, due to the large variety of models encountered, forward modeling algorithms must be robust and resilient to artifacts. The setting for my San Emidio line 6 models is a 2D cartesian coordinate space (x, z), where x is defined as distance easting and z as depth. Each element in the model space has dimensions of 17 m by 17 m (55 ft by 55 ft), with the origin defined as the shallowest western corner element.

The deterministic Vidale method generates my traveltime models through a finite-difference solution to the eikonal equation (Vidale, 1988). Visual examination of isotime contour plots shows that my traveltime model produces accurate results amidst the most extreme velocity gradients encountered during optimization.

Gravity modeling must be compatible with the model space of the Vidale method and meet the demands of being both efficient and robust. My gravity model obtains a 3D gravitational response from 2D density models, which Fedi et al. (1998) term 2.5D modeling. Telford and Sheriff (1990) point out that this type of extrapolation is only valid when variation in and out of the plane in minimal; examining directional gravity gradients shows this to be a reasonable assumption. The derivation and verification of my gravity model can be found in Reeder et al. (2014). One difference between my final model and the one shown in Reeder et al. (2014) is that the gravity model used in this study employs the line integral method of Talwani et al. (1959) instead of infinite cylinders.

Hubbert (1948) showed that the vertical component of an arbitrary polygon's gravitational response is given by a line integral along the boundaries with respect to the angle θ, which is measured from the positive (downward) z-axis to the positive (eastern) x-axis. The integral can be decomposed into n separate integrals from the points A to B, where n is the number of polygon vertices (Equation 2.1). My

numerical implementation follows Talwani et al. (1959).

$$g_z = 2G\rho \sum_{i=1}^{n} \int_{A_i}^{B_i} z \; d\theta = 2G\rho \sum_{i=1}^{n} \int_{A_i}^{B_i} \frac{\alpha_i tan\theta_i tan\phi_i}{tan\phi_i - tan\theta_i} \; d\theta \tag{2.1}$$

2.2.6 Simulated Annealing Algorithm

The SA technique has been applied to a wide variety of optimization problems, including circuit design, chemical processing, facility layout design, pattern recognition, and wavefield inversion (Basu and Frazer, 1990; Suman and Kumar, 2005). SA takes its name from the annealing process of petrology and metallurgy, which describes how rock crystallizes from a melt. In contrast to local optimization algorithms, SA probabilistically accepts models with higher error; this mechanism allows the algorithm to escape local minima. One of the benefits of this technique is that it does not depend on an accurate initial model, which is very useful in areas of complex geology with limited a priori information.

The idea of probabilistic acceptance of higher error models during optimization was first put forth by Metropolis et al. (1953). More than thirty years later, Kirkpatrick et al. (1983) and Černý (1985) independently took the idea one step further by slowly decreasing the probabilistic acceptance chance, which is colloquially known as lowering the temperature. Szu and Hartley (1987) and Beaty et al. (2002) improved efficiency with 'fast' SA, which draws new models from a Cauchy-Lorentz distribution instead of a Gaussian distribution. Next, Zhang et al. (1997) and Ingber (1993) presented 'very fast' SA, which narrows the range of possible models through iterations. Chunduru et al. (1997) utilize a hybrid SA optimization technique that occasionally draws a new model using gradient descent. Yang et al. (2002) present 'improved very fast' SA, which utilizes a 'double judge' error-checking rule to prevent joint optimization objective function errors when using 'very fast' SA. Since efficiency is outside the scope of this paper, my implementation of the generalized SA algorithm follows the outline of Pullammanappallil (1994), who first applied this optimization technique to first arrival traveltime tomography.

Model depth of 1,526 m (5,005 ft) is based on a-priori information of maximum bedrock depth from wells. The allowed velocity range of 500 m/s to 6,500 m/s (1,600 ft/s to 21,000 ft/s) comes from previous velocity modeling results and rock physics estimations. Before optimization commences, each model element is populated with a random velocity, followed by running a set number of iterations at supraliquidus temperatures to achieve a state of high disorder prior to cooling (e.g., Pullammanappallil (1994)). The velocity model is converted into a density model using my extended Gardner's relationship (Figure 2.5). Starting traveltime and gravity models are obtained, followed by calculation of root-mean-square error σ as follows:

$$\sigma = \sqrt{\frac{\sum_{i=1}^{n_x}(x_i^{observed} - x_i^{calculated})^2}{n_x}} \tag{2.2}$$

n_x represents the total number of measurements. Seismic and gravity error values are calculated separately. The velocity model is perturbed by setting a random rectangular region of the model to a random velocity. Afterwards, the updated velocity model is converted to a density model and new energies are calculated. The standard and conditional model acceptance criteria are given as follows:

$$if \;\; (\sigma_{ns} < \sigma_{os}) \; AND \; (\sigma_{ng} < \sigma_{og}) \tag{2.3}$$

$$elseif \;\; e^{\frac{(\sigma_{ss}-\sigma_{ns})^q(\sigma_{os}-\sigma_{ns})}{T_s}} > rand[0,1] < e^{\frac{(\sigma_{sg}-\sigma_{ng})^q(\sigma_{og}-\sigma_{ng})}{T_g}} \tag{2.4}$$

Where rand[0,1] is a random number from 0 to 1; σ_{ns} and σ_{ng} represent the 'daughter' model errors for seismic and gravity, respectively; σ_{os} and σ_{og} are the 'parent' errors; σ_{ss} and σ_{sg} are the 'successful' errors; T_s and T_g are the temperatures; and q is an even whole number that is determined empirically. If either of the aforementioned logical expressions are true, the daughter errors and models replace the parent. σ_{ss} and σ_{sg} equal the measurement error in seismic and gravity data, which is also used in the stopping criteria; setting σ_{ss} and σ_{sg} equal to less than measurement errors would allow χ^2 values less than 1, which would permit model overfitting (Van Avendonk et al., 2001). Finally, the algorithm checks all stopping criteria; these include maximum number of iterations, successful error, minimum temperature, and maximum

number of successive model rejections. If no stopping criteria are met, the cooling schedule is exercised and the algorithm loops back to the model pertubation step. This process continues until a stopping criteria is met.

The most impactful component of a joint optimization is the objective function (Roy et al., 2005). This is where Tikonov regularization can be implemented, such as damping (Snieder and Trampert, 2000), smoothness (Constable et al., 1987; Boulanger and Chouteau, 2001; Vermeesch et al., 2009; Berger et al., 2011; Lelièvre et al., 2012), or structural similarity (Xiao et al., 2011; Teranishi et al., 2012; Haber and Holtzman Gazit, 2013). My optimization does not include additional constraints on the objective function nor a priori information, but my objective function does use different seismic and gravity temperatures.

The temperatures, T_s and T_g, are in the denominator of the exponentials; as T_s and T_g decrease, the probability of both exponentials being greater than rand[0,1] tends towards zero. The seismic temperature (T_s) is converted into a gravity temperature (T_g) at each step. The conversion factor is determined through a novel calibration technique that uses Pareto charts (Figure 2.6). Suman and Kumar (2005) provide a comprehensive overview of Pareto optimization. In this application, the Pareto chart shows whether the seismic or gravity component of the objective function is dominating the optimization. I found that seismic-gravity objective function balance occurs when gravity temperatures (T_g) are equal to the iteration-equivalent seismic temperatures (T_s) divided by 100,000 (Figure 2.6b). However, this value is model dependent.

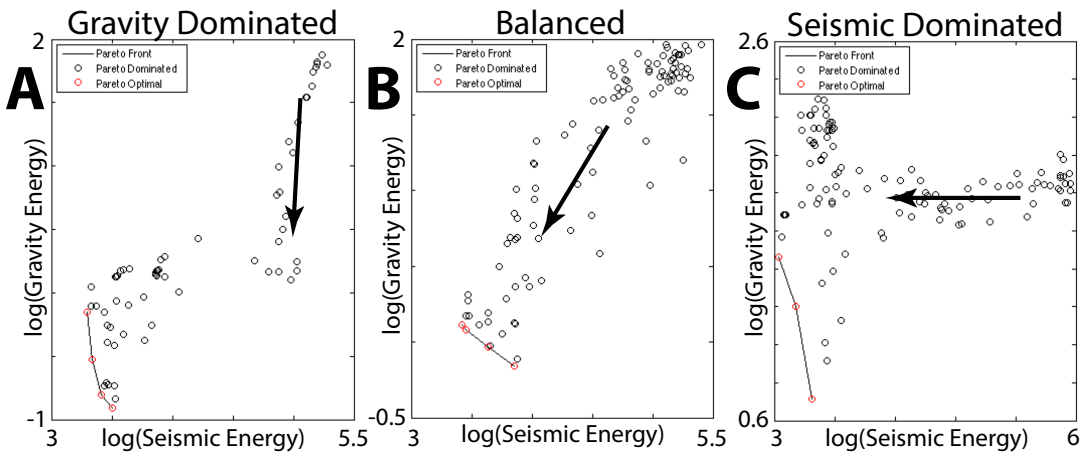

Figure 2.6: Three types of Pareto charts, with arrows indicating the trend through iterations. Each circle represents an average over 5,000 iterations. **(A)** Gravity-dominated Pareto chart, which indicates an increase in the seismic-to-gravity temperature conversion factor is needed. **(B)** Balanced Pareto chart, which indicates the joint optimization is well-calibrated. **(C)** Seismic-dominated Pareto chart, which can be resolved by decreasing the seismic-to-gravity temperature conversion factor.

The cooling schedule, which controls the probabilistic acceptance criteria, consists of an initial temperature, temperature reduction scheme, critical temperature, and minimum temperature. The choice of an effective cooling schedule is very important; for example, Basu and Frazer (1990) show that it is cost-effective to use 80% of total computation budget on determining the critical temperature alone. Lee and Lee (2013) conclude that there is still work to be done towards an analytical determination of an optimal starting temperature, but as long as the initial temperature is set sufficiently high, achieving the global minima is possible. The effective temperature range is mapped utilizing ideas taken from Basu and Frazer (1990). Short tests (1,000 iterations) over a discretized temperature series ranging from 10^{100} to ~ 0 establish the liquidus and solidus (Figure 2.7). The liquidus boundary occurs at a temperature of $10^{5.5}$, while the solidus – where probabilistic acceptance tends to zero – is located at $10^{2.6}$.

The critical temperature is a fixed temperature across many iterations that occurs just before reaching the solidus. For single objective functions, Basu and Frazer (1990) present a very effective method of critical temperature determination, in which a series

of tests are run at static temperatures to find where error is minimized. However, their method is not effective for a joint seismic-gravity objective function. My final joint optimization critical temperature of $100^{2.8}$ is deduced empirically by exploring values slightly above the solidus; this value is model-dependent, and must be rederived when new observations are used. Upon discovery of the critical temperature, similar testing is carried for the value of q that minimizes error, which is equal to 2.

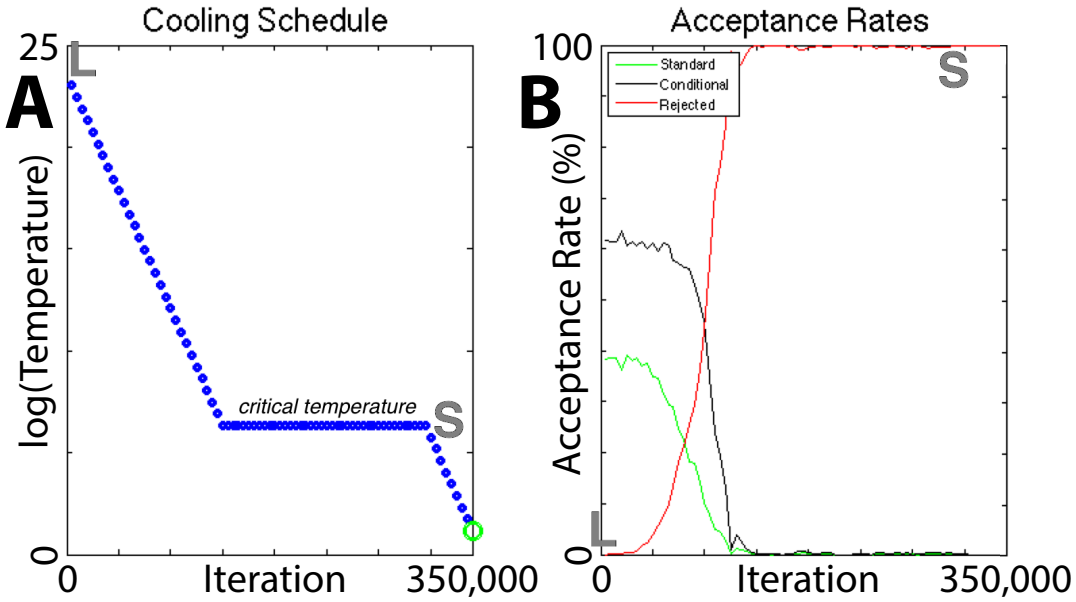

Figure 2.7: Results of a joint optimization cooling study. **(A)** Cooling schedule. Tested temperatures are given by blue circles, with the final temperature given by a green circle. The liquidus and solidus are indicated by 'L' and 'S', respectively. The critical temperature is labeled; in this case the optimization stayed at that temperature for 200,000 iterations. **(B)** Acceptance rate plots. The standard and probabilistic acceptance rates are given by green and black lines, respectively. The rejection rate, indicated by a red line, begins at 0% and increases to just below 100% at the critical temperature. The rejection rate is 0% while the temperature is above the liquidus ('L') and reaches 100% at the solidus ('S').

2.2.7 Kirchhoff Prestack Depth Migration Algorithm

The most straightforward way to judge the quality of two velocity models is by comparing the magnitude of traveltime misfits. However, a lower error does not necessarily mean a velocity model is *better*. Comparing coherency of migrated seismic sections

allows further analysis of velocity model quality. The Kirchhoff prestack depth migration (KPSDM) code aaRGkmig.c creates my seismic images (Louie, 2014, Personal Comm.). KPSDM has proven effectiveness in areas with sharp lateral velocity variations (Louie et al., 1988; Louie and Qin, 1991; Honjas and Pullammanappallil, 1997; Chávez-Pérez et al., 1998; Louie et al., 2012). KPSDM has been described as a ray-equation back-projection inversion of the acoustic wave field (Louie et al., 1988). Three assumptions are inherent to this technique: the Born approximation, the WKBJ approximation, and the far field assumption. The Born approximation assumes that reflections are caused by rapid variation in material properties and data only include primary reflections. The WKBJ approximation, also known as the geometric optics approximation, implies seismic energy propagates along infinitely high-frequency rays through material with properties that vary slowly (Robinson, 1986). This facilitates solving the wave equation and grants low-frequency energy unrealistic sensitivity to thin refractors (Brown, 1982). The far field assumption implies receivers are at least two wavelengths away from sources, which precludes the inclusion of complex near-field diffraction interactions.

The aaRGkmig.c code includes operator anti-aliasing as described by Lumley et al. (2012), the obliquity factor of Claerbout (1985), and the kirchfast speedup described in Claerbout (1997). Setting the anti-aliasing distance parameter equal to the shot spacing (67 m or 220 ft) produces less noisy migrations than using the receiver spacing (17 m or 55 ft). I generate traveltime planes using the algorithm described in Vidale (1988). Since migration resolution is equivalent to the resolution of input traveltime planes, I conduct testing to ensure image aliasing does not occur. Preferred model dimensions are 195 easting elements by 91 depth elements. Each element is square with dimensions of 17 m by 17 m (55 ft by 55 ft). After migration, I apply the rho filter of Thorson and Claerbout (1984), which consists of two time-derivatives followed by element-wise multiplication by -1; this is colloquially known as a frequency recovery filter (Figure 2.4). I then smooth the migration image with a 3 by 3 smoothing kernel. This combination acts to suppress low-frequency summation

artifacts and short-wavelength noise, while preserving reflectors of interest.

2.3 Results

My results come from one seismic line collected at one geothermal field. The geologic setting of my survey is typical of most geothermal resources in the Great Basin, suggesting general applicability of this method. Comparisons between seismic SA optimization and joint seismic-gravity SA optimization are made using synthetics, but these tests do not make use the same proprietary seismic SA features of SeisOpt® Pro™.

2.3.1 Synthetic Testing

Synthetic testing shows how joint optimization further constrains velocity models. The synthetic velocity model consists of a bedrock interface with two downward steps (Figure 2.8a). Gardner's relation converts the synthetic velocity model into a density model. A gravity model is generated using the synthetic density model, followed by density optimization using SA (Figure 2.8b). Traveltime optimization is performed on generated synthetic traveltimes (Figure 2.8c). Joint optimization is used to obtain a velocity-density model from the synthetic traveltimes and gravity model (Figure 2.8d).

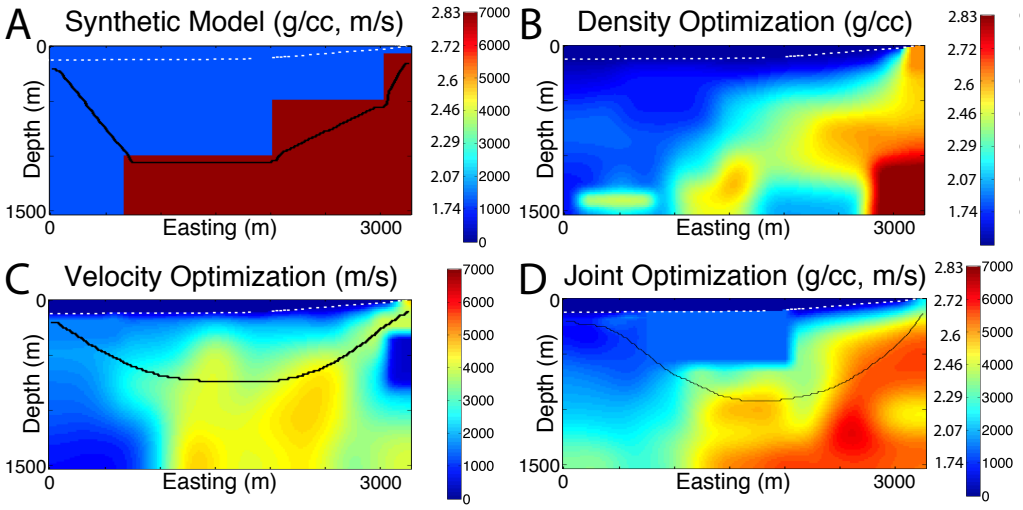

Figure 2.8: Results of the synthetic testing study. **(A)** Synthetic velocity model. Sediments have a velocity of 1,500 m/s (4,900 ft/s) and the bedrock has a velocity of 6,500 m/s (23,000 ft/s). Corresponding densities are 1.93 g/cc and 2.78 g/cc. **(B)** Gravity optimization results with an RMS error of 0.41 mGal. **(C)** Seismic optimization results, which have an RMS error of 33.7 ms. **(D)** Joint seismic-gravity optimization with RMS errors of 102.6 ms for seismic and 2.56 mGal for gravity.

Gravity optimization successfully recovered the shallow structure and general trend of down-to-the-west bedrock with an RMS error of 0.41 mGal (Figure 2.8b). However, gravity optimization produces a strong density inversion near the bottom of the model. Seismic optimization produces a models with insufficiently high velocities that are diffused through the model space and an RMS error of 33.7 ms (Figure 2.8c). The shallow velocity inversion on the east side of the velocity model is below the deepest ray; typically, everything below the deepest ray would be clipped and the empty elements in the remaining rectangular model space would be populated by model extension. Qualitatively, joint optimization most successfully recovered the synthetic model, but showed higher RMS errors of 2.56 mGal and 102.6 ms (Figure 2.8d). These results show that my joint optimization is superior to my stand-alone seismic and gravity optimizations, but has higher RMS error.

2.3.2 Plotrefa^{TM} Velocity Model

Plotrefa^{TM} produces a velocity model with a flat valley floor (Figure 2.9a), a prominent shallow velocity pull-up (Figure 2.9b$_2$), and a blocky alluvium-bedrock interface. Elements near the flat valley floor assume the velocity distribution of the initial model, as this area is below the deepest raypath, and was not updated across iterations (Figure 2.9a). The RMS error of this model is 13 ms and the corresponding χ^2 value is 1.94; this indicates that the model underfit the data by converging to a local minima. Reflectors in the shallow western part of the migration are arcuate and lack strong coherency (Figure 2.10b$_1$). A shallow velocity pull-up results in pronounced antiformal deformation of the shallow reflector in the migration image (Figure 2.10b$_2$). The two vertical discontinuities separating horizontal bedrock in the velocity model suggest the presence of vertical, down-to-the-west normal faults (Figure 2.9). However, this observation does not match reflectivity in the migration (Figure 2.10). Subtle reflectivity is observed on the eastern edge of the migration at 500 m (1,600 ft) depth (Figure 2.10d$_1$). This reflectivity has increasing wavelength towards the eastern edge of the model caused by NMO stretch. Reflectors in the migration generally lack coherency, which can be attributed to an abundance of high-amplitude cross-cutting migration artifacts (Figure 2.10a, b$_1$, c, d$_2$).

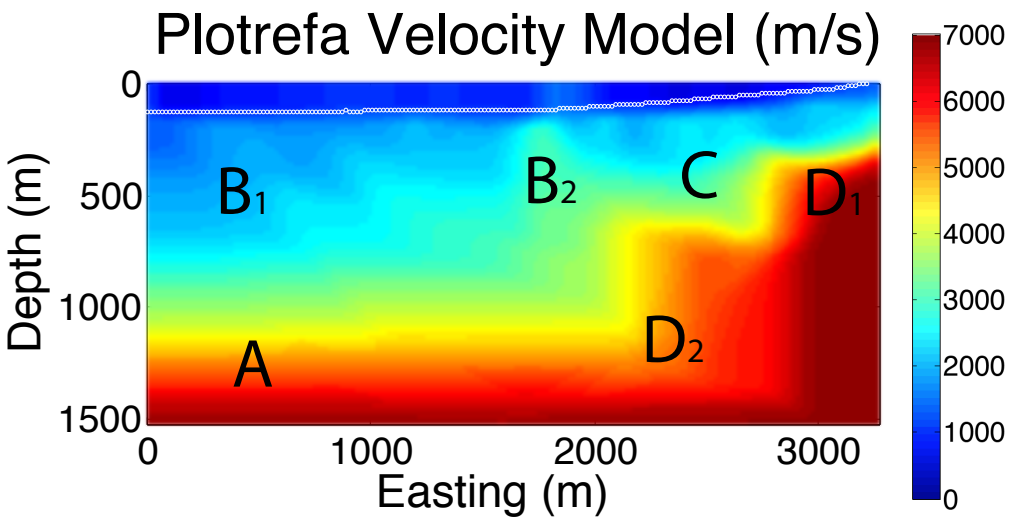

Figure 2.9: Plotrefa^{TM} velocity model with receiver locations indicated by white circles. **(A)** Deep velocity gradient indicating the sediment-bedrock contact. **(B_1)** Velocities consistent with sediment. **(B_2)** Shallow velocity pull-up. **(C)** Shallow velocity gradient indicating the sediment-bedrock contact. **(D_1)** Velocities consistent with igneous rock. **(D_2)** Velocities consistent with igneous rock.

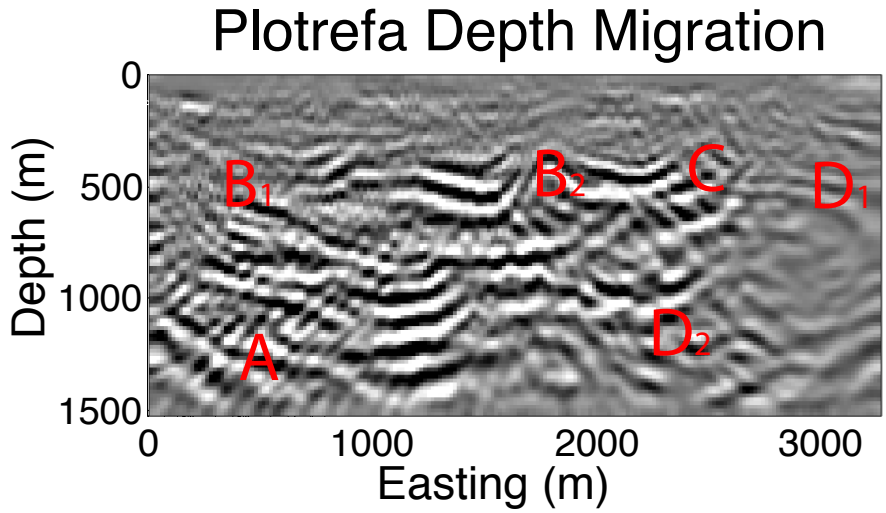

Figure 2.10: Migration using the Plotrefa^{TM} velocity model. **(A)** Deep, arcuate reflector with low coherency. **(B_1)** Shallow reflector that dips to the east. **(B_2)** Shallow antiformal reflector. **(C)** Shallow, incoherent reflector **(D_1)** Shallow reflector that intersects the edge of the migration. **(D_2)** Incoherent deep reflector.

2.3.3 SeisOpt® Pro™ Velocity Model

The SeisOpt® Pro™ velocity model shows a flat valley floor (Figure 2.11a), shallow velocity pull-up (Figure 2.11b$_2$), and a jagged sediment-bedrock interface that generally dips to the west at 30°. The RMS error for this model is 6.5 ms; this gives a χ^2 value of 0.97, indicating these data are slightly overfit. The velocity gradient is very sharp on the western side of the velocity model at 1,400 m (4,600 ft) depth; this region was populated by manual lateral model extension. This sharp gradient corresponds to a concave and highly coherent deep valley reflector (Figure 2.12a). Shallow reflectors on the west side of the migration are incoherent (Figure 2.12b$_1$). Antiformal deformation of a shallow reflector is congruent with the shallow velocity pull-up (Figures 2.11b$_2$ and 2.12b$_2$). The continuous shallow reflector observed in the Plotrefa™ migration is now truncated on the east side (Figure 2.12d$_1$), while the deep reflector is more coherent, but lower amplitude (Figure 2.12d$_2$).

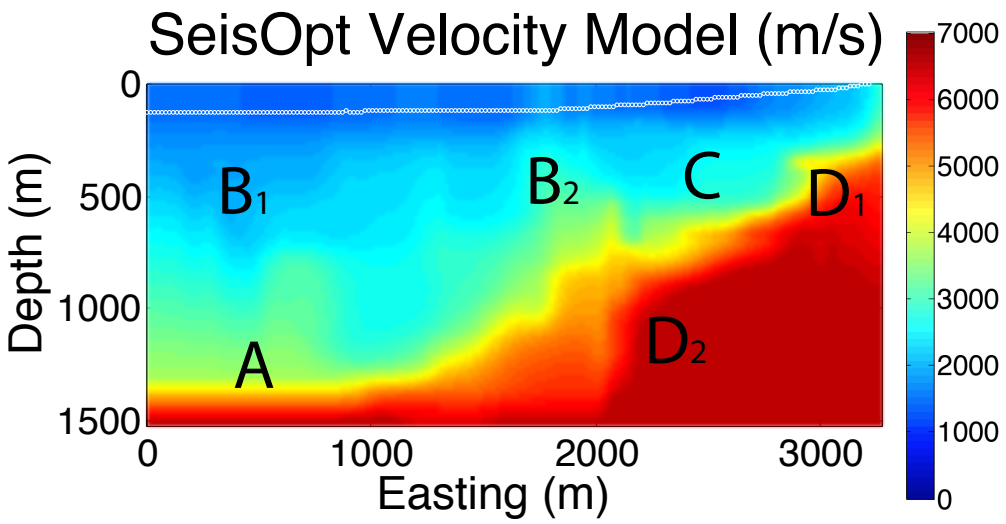

Figure 2.11: SeisOpt® Pro™ velocity model with receiver locations indicated by white circles. **(A)** Deep velocity gradient indicative of the sediment-bedrock interface. **(B_1)** Velocities consistent with sediment. **(B_2)** Shallow velocity pull-up. **(C)** Velocities consistent with sediment. **(D_1)** Shallow velocity gradient caused by the sediment-bedrock contact. **(D_2)** Velocities consistent with igneous rock.

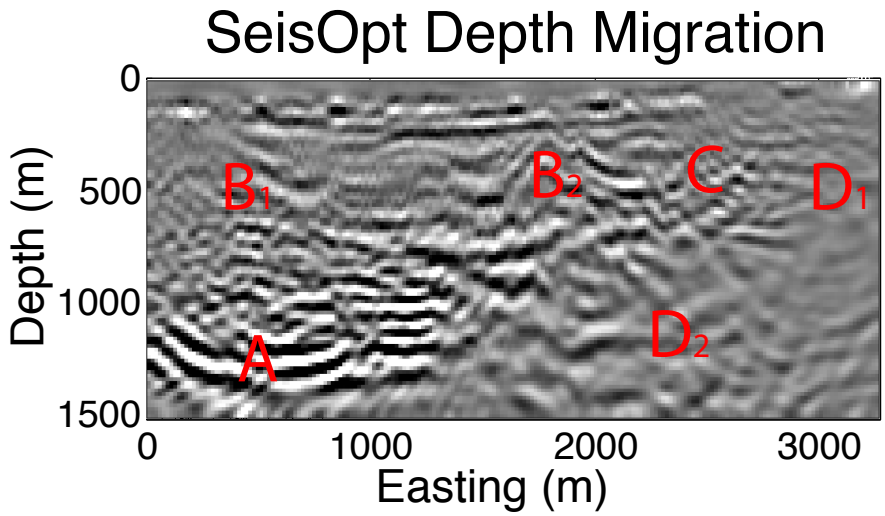

Figure 2.12: Migration using the SeisOpt® Pro™ velocity model. **(A)** Deep, concave reflector with good coherency. **(B_1)** Incoherent shallow reflector. **(B_2)** Shallow antiformal reflector. **(C)** Incoherent shallow reflector **(D_1)** Shallow reflector that is truncated on the east side. **(D_2)** Incoherent deep reflector.

2.3.4 Joint Seismic-Gravity Optimization Velocity Model

Joint optimization provides a velocity model with an absence of a deep valley bedrock interface (Figure 2.13a), minor velocity inversions (Figure 2.13b_1, d_2), and a smooth, convex bedrock profile (Figure 2.13c). The RMS error for gravity is 1.25 mGal and 27 ms for seismic traveltimes; this gives a χ^2 value of 4, indicating that this velocity model noticeably underfits first arrival data. On the westernmost side, velocities consistent with sedimentary rock extend from the surface to the bottom of the velocity model; this suggests the valley is deeper than 1,500 m (4,900 ft) (Figure 2.13a). Reflectors on the west side of the migration are straight and coherent (Figure 2.14a, b_1). The sediment-bedrock velocity interface has a westward dip of 20° on the eastern margin, which gradually increases to a dip of 60° near the center of the model (Figure 2.13c). The top side of this velocity gradient is congruent with a very coherent reflector (Figure 2.14c). Minor velocity inversions occur in valley fill at 500 m (1,600 ft) depth on the west side (Figure 2.13b_1) and at 1,200 m (3,900 ft) depth in the bedrock (Figure 2.13d_2). In this migration, the shallow antiformal reflector observed in the Plotrefa™ and SeisOpt® Pro™ migrations is flat (Figure 2.14b_2). The truncated shallow reflector on the east side (Figure 2.14d_1) is now intersected by subtle reflectors that dip westward at 45°. These dipping reflectors transition to horizontal westward forming a highly coherent, long-wavelength deep reflector (Figure 2.14d_2).

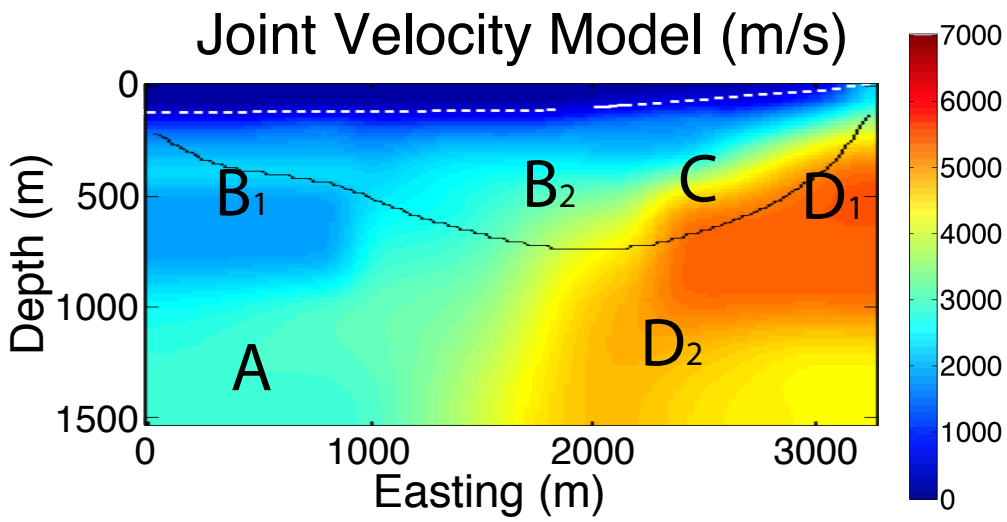

Figure 2.13: Joint seismic-gravity optimization velocity model result with source locations indicated by white rectangles. **(A)** Velocities consistent with lithified sediment. **(B_1)** Shallow velocity inversion in sediment velocities. **(B_2)** Weak velocity gradient from sedimentary to igneous velocities. **(C)** Strong velocity gradient from sediment to igneous rock. **(D_1)** Velocities consistent with igneous rock. **(D_2)** Deep velocity inversion with igneous rock velocities.

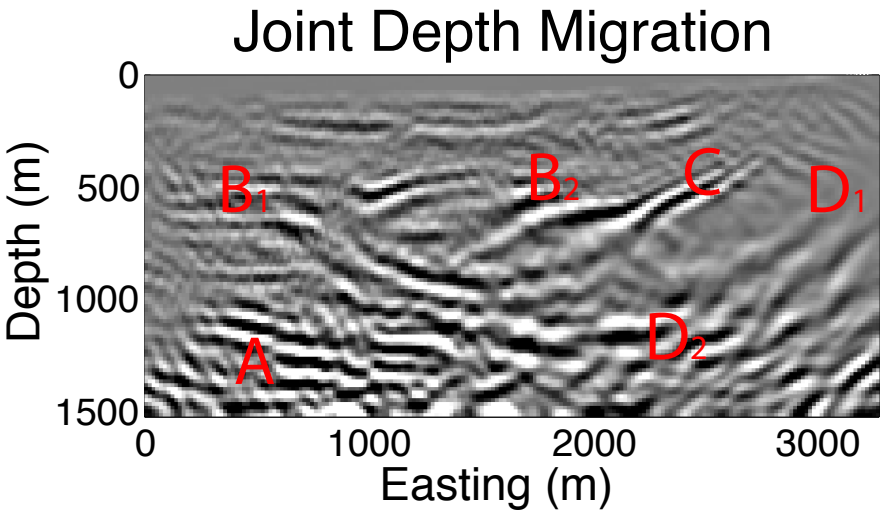

Figure 2.14: Migration using the velocity model created through joint optimization. **(A)** Coherent, straight deep reflectors. **(B_1)** Shallow horizontal reflector. **(B_2)** Shallow horizontal reflector **(C)** Coherent shallow reflector that dips to the west. **(D_1)** Shallow reflector that is truncated on the east side. **(D_2)** Deep, long-wavelength reflector with moderate coherency.

2.3.5 Restricted Offset Range Migrations

Restricted offset range migrations of the SeisOpt® Pro™ velocity model (Figure 2.11) reveal which offset ranges the reflector energy in my final migration images is coming from (Figure 2.15). Empirically, there are three discernable effective offset ranges; the 'near' offset range of 0 m to 1,500 m (0 to 4,900 ft) (Figure 2.15I); the 'mid' offset range of 1,500 m to 2,000 m (4,900 ft to 6,600 ft) (Figure 2.15II); and the 'far' offset range of 2,000 m to 3,200 m (6,600 ft to 10,600 ft) (Figure 2.15III).

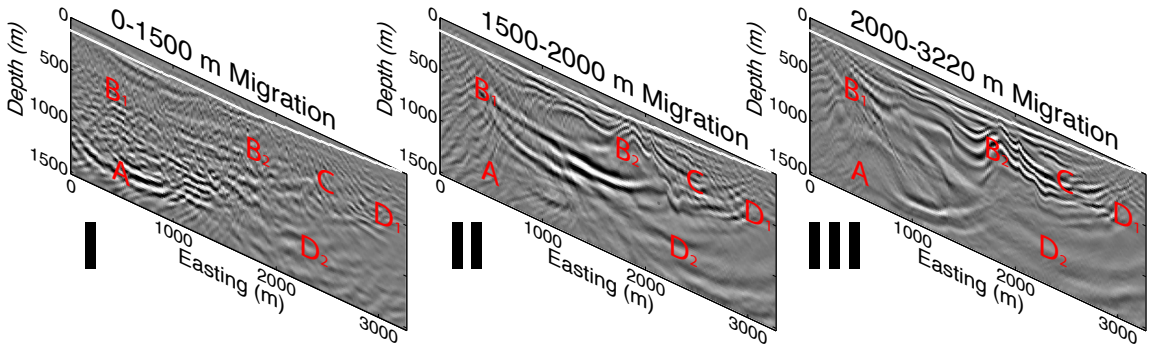

Figure 2.15: Results of the restricted offset range migration analysis. **(I)** Near-offset migration from 0 m to 1,500 m (0 ft to 4,900 ft). **(II)** Mid-offset migration from 1,500 m to 2,000 m (4,900 ft to 6,600 ft). **(III)** Far-offset migration from 2,000 m to 3,200 m (6,600 ft to 10,600 ft).

The near-offset migration contains the deep valley reflector (Figure 2.15I-a), deep basement reflector (Figure 2.15I-d_2), and minor shallow reflector energy (Figures 2.15I-b_1 and 2.15I-d_1). The mid-offset migration contains a high amplitude concave reflector in the center, part of the deep basement reflector energy (Figure 2.15II-d_2), highly sinuous shallow reflector energy (Figure 2.15II-b_2), and a smooth, concave shallow reflector (Figure 2.15II-c). The far-offset migration is dominated by the highly sinuous shallow reflector energy (Figure 2.15III-b_2) that transitions eastward into the smooth shallow reflector (Figure 2.15III-c).

2.4 Discussion

2.4.1 Geologic Interpretations

The flat valley floor interpretation that would naturally come from the Plotrefa™ (Figure 2.9a) and SeisOpt® Pro™ (Figure 2.11a) velocity model results is not supported by seismic data, as that region of the velocity model is below the deepest headwave raypath, and is therefore unconstrained. In the case of Plotrefa™, this region matches the initial model, as it was not subjected to model pertubation. For the SeisOpt® Pro™ results, the deep valley velocity gradient is purely a function of arbitrary lateral model extension from the deepest raypath. Since I observed that creating a concave refractor using vertical model extension produces arrival times that are too early, the bedrock interface must not be shallowing substantially on the west side of the velocity model. Reflectors in this area are incoherent in the migration using the Plotrefa™ velocity model and arcuate in the migration using the SeisOpt® Pro™ velocity model (Figures 2.10a and 2.12a). The added deep velocity control from gravity in the joint optimization results in a velocity model that shows the valley being at least 1,500 m (4,900 ft) deep (Figure 2.13a). The reflectors in this region also become flat and coherent when the jointly optimized velocity model is used for migration, which is expected for undeformed Tertiary sediments (Figure 2.14a). Most of the energy in these reflectors comes from robust near-offset data (Figure 2.15I-a). The deep valley model that results from joint optimization conflicts with the prior shallow valley interpretation of Rhodes (2012), who was basing his interpretations on surficial geologic mapping. My new interpretation could be validated by conducting a seismic survey with greater maximum offset or comparing to well log data. Matlick (1995) reports that Chevron's Kosmos 1-8 well, which is located 700 m north of the western edge of line 6, did not encounter Mesozoic basement rock (Nightingale formation) at target well depth of 1,223 m (4,013 ft).

Convex velocity pull-ups in the Plotrefa™ (Figure 2.9b$_2$) and SeisOpt® Pro™ (Figure 2.11b$_2$) velocity models translate to antiformal reflectors in corresponding

migrations (Figures 2.10b$_2$ and 2.12b$_2$). Incidentally, a similar velocity pull-up is observed in the synthetic traveltime optimization, because velocities are spread along sparse rays in all of these cases (Figure 2.8c). Vasco et al. (1996) shows that sharp velocity interfaces can be equivalently represented by models with lower magnitude velocity gradients that diffuse velocity contrasts over a broader region. The creation of these features in Plotrefa^{TM} can also be explained by the way that the velocity model is perturbed along concave raypaths; the prominent velocity pull-up follows an area of high ray coverage density and sharp velocity gradients (Geometrics, 2009). This antiformal reflector is flattened when the jointly optimized velocity model is used for migration (Figure 2.14b$_2$). As shown in the synthetic models, density optimization was most effective at recovering shallow structure (Figure 2.8b). The flattening of this shallow reflector demonstrates that including gravity constraints in the velocity optimization improves the resolvability of shallow velocity structure. This constraint is caused by the decay of gravity sensitivity as the inverse of the distance squared; gravity models are very sensitive to shallow density model elements. Furthermore, shallow reflectors on the western side of the model are more straight and coherent when the joint optimization velocity model is used for migration (Figure 2.14b$_1$). Restricted offset range migrations reveal that the sinuous shallow reflectors are primarily found in offsets greater than 1,500 m (4,900 ft); this suggests that these reflectors may just be migrated refraction energy instead of true reflectors (Figures 2.15II-b$_2$ and 2.15III-b$_2$). This also helps explain the sensitivity of the antiformal reflectors to the input velocity model (Figures 2.9b$_2$, 2.11b$_2$, and 2.13b$_2$). On the contrary, the presence of this reflector is well-established by drilling; Matlick (1995) states that Phillips ST-1 intersected the sediment-basalt contact roughly 250 m (820 ft) south of line 6 at an easting of 1,700 m (5,700 ft) and depth of 485 m (1,590 ft). This lithological contact is found within 75 m (250 ft) of the shallow reflector in all of my migrations (Figures 2.10b$_1$, 2.12b$_1$, and 2.14b$_1$). The sensitivity of these reflectors to the velocity model and lack of presence in near-offset migrations suggests that this contact may be gradational in nature, which produces pseudoreflections or diving waves. The sinuous

reflector at 500 m (1,600 ft) depth and 2,500 m (8,200 ft) easting is most coherent in the migration using the jointly optimized velocity model (Figure 2.14c), in which this reflector corresponds to a sharp velocity gradient (Figure 2.13c). This shallow reflector is incoherent in the Plotrefa™ and SeisOpt® Pro™ migrations (Figures 2.10c and 2.12c), and is not congruent with sharp velocity gradients (Figures 2.9c and 2.11c). This is further evidence that joint optimization improves shallow regions of velocity models. Restricted offset range migrations indicate that this reflector is primarily concentrated in the far offsets; this could actually be a pseudoreflector (diving wave) caused by the velocity gradient (Figure 2.15). This is strong evidence for a velocity gradient in this region of the model space. Typically, smoothing shallow reflectors can be accomplished by manual refinement of the velocity model or by migration velocity analysis; using joint optimization removes the need for this step, saving human interaction time.

Applying knowledge of the well control given by Phillips ST-1 reveals that the reflector at b_2 and c is very likely the alluvium-basalt interface. The stratigraphic column suggests that the next deeper reflector should be a basalt-tuff interface, followed by a tuff-basement reflector. None of the migrations demonstrate the basalt-tuff reflector, due to the fact that theoretically it is a weakly negative impedance contrast. Mayhew (2013) also could not differentiate the basalts and tuffs in seismic migrations at nearby Astor Pass; this seismic facies was verified by subsequent drilling. However, evidence for the basement interface is observed. The first line of evidence are reflection terminations in both the SeisOpt® Pro™ and jointly optimized velocity model migrations at the depth-projected position of the mapped surficial rangefront fault (Figures 2.12d_1 and 2.14d_1). Following the surficial fault project deeper reveals a strong, slightly concave reflector that appear offset (Figure 2.14d_2). The deep reflector interpreted to be the tuff-basement contact is poorly resolved in the migrations that use Plotrefa™ and SeisOpt® Pro™ velocity models (Figures 2.10d_2 and 2.12d_2). This region is situated below the deepest first-arrival raypath, and is therefore unconstrained by standard velocity modeling techniques; this indicates that

joint optimization produces a more accurate velocity model at depth, which helps focus the seismic image below the basalt refractor.

Two velocity inversions are observed in the jointly optimized velocity model (Figure 2.13b_1, d_2). The shallow rectangular velocity inversion at Figure 2.13b_1 corresponds to flat reflectors in the migration image (Figure 2.14b_1). These flat reflectors are not very coherent in the Plotrefa™ (Figure 2.9b_1) and SeisOpt® Pro™ (Figure 2.11b_1) migrations. Most of this shallow velocity inversion is below the deepest raypath, but these shallow elements are very sensitive to the gravity component of the the joint optimization; this suggests that this shallow velocity inversion may be real. Assuming that the shallow reflector discussed earlier is the sediment-basalt contact, the deep velocity inversion at the bottom of the jointly optimized velocity model is situation stratigraphically in the Mesozoic section (Figure 2.13d_2). This velocity inversion is below the deepest raypath, poorly constrained in the gravity model, and does not correspond to reflectors. For these reasons, this velocity inversion is most likely an artifact of joint optimization. Implementing regularization could resolve this artifact. In the end, the deep velocity inversion does not have a meaningful impact on the resultant migration image (Figure 2.13d_2).

Previous researchers in the Pyramid Lake area have shown that blind geothermal systems tend to exist on north-northeast trending normal faults in highly faulted areas, such as fault intersections and fault tips (Drakos, 2007; Vice, 2008; Rhodes, 2012; Mayhew, 2013; Anderson, 2013). Phillips ST-1 intersected a major fault 200 m (660 ft) south of line 6 at an easting of 1,700 m (5,700 ft) and depth of 588 m (1,930 ft). This fault is not well-resolved in my migration images (Figures 2.10b_2, 2.12b_2, and 2.14b_2). However, Mayhew (2013) states that the Pyramid sequence rocks that this fault cuts are too permeable to focus fluid motion through faults; he suggests that the real target should be fault intersections in the Mesozoic basement. The migration that uses a velocity model produced by joint optimization successfully imaged a fault in the Mesozoic section (Figure 2.14d_1). Reflector truncations around the area of 1,200 m (3,900 ft) easting and 1,100 m (3,600 ft) depth in migrations using velocity

models produced by SeisOpt® Pro™ and jointly optimization could be produced by a fault contact of Tertiary sediments adjacent to volcanic rocks (Figures 2.12, and 2.14). This fault could be the Mesozoic conduit for fluids that Mayhew (2013) suggests looking for.

Rhodes (2012) mapped a surficial down-to-the-west normal fault 100 m (330 ft) east of the eastern edge of my model space. Assuming this fault has a 60° dip that projects into the surface, the bedrock interface dips too shallowly in all of my velocity models (Figures 2.9, 2.11, and 2.13). The easternmost edge of the velocity model has very low fold and is poorly constrained, particularly at depth. When gravity constraints are added, a deep reflector is observed dipping to the west (Figure 2.14) that could be projected to the surface location of the rangefront fault in Rhodes (2012). This reflector is concave and flattens westward from 45° to 0° from Figure 2.14d_1 to Figure 2.14d_2, suggesting that this normal fault is listric. This reflector shows a breach in coherency at 2,000 m (6,500 ft) easting and 1,300 m (4,300 ft) depth, which could indicate another fault in the Mesozoic section. Given that the Oligocene and Miocene sections dip to the east at 20°, the hydrothermal fluids could be concentrated in this Mesozoic fault before following stratigraphic boundaries up and to the west. Upon reaching the Tertiary clastic section, the fluids could be rising up, creating the current production zone discovered by Phillips ST-1. This production zone is located within the region of gradational velocity suggested by pseudoreflections (Figure 2.13b_2).

2.4.2 Implications

The efficiency of joint optimization is comparable to Plotrefa™ and SeisOpt® Pro™. The final run of Plotrefa™, which consisted of just 14 total iterations, took roughly 13 hours; the bulk of this time was used for matrix inversion. The run of SeisOpt® Pro™ took 16 hours. I completed all joint optimizations in under 20 hours, with the time requirement depending on the number of iterations specified. I greatly improved the efficiency of the joint optimization by the inclusion of Matlab MEX codes, which takes advantage of the C language, and by vectorization of 'for' loops.

Further efficiency improvement can be obtained by porting my optimization to C.

Comparing the RMS errors of jointly optimized velocity models to Plotrefa™ and SeisOpt® Pro™ reveals that joint optimization produces higher RMS errors. Traveltime RMS error are 6.5 ms for SeisOpt® Pro™, 13 ms for Plotrefa™, and 27 ms for my joint optimization. Only SeisOpt® Pro™ produces a velocity model with a χ^2 value below unity, while the other two techniques both underfit data. Using this criteria, SeisOpt® Pro™ performed the best. Lower RMS errors could be achieved with the joint optimization by also optimizing the coefficients of the velocity-to-density conversion polynomial; it is possible that using the Gardner relationship causes inconsistencies between the gravity and seismic datasets. However, similar results are observed in the synthetic models, which uses a flawless' velocity-to-density conversion; the synthetic velocity optimization has an RMS error of 33.7 ms, while the synthetic joint optimization has an RMS error of 102.6 ms. This indicates that adding gravity constraints comes at the cost of seismic RMS error. Qualitatively comparing the optimized synthetic velocity models suggests that joint optimization produces superior results to traveltime optimization alone, which suggests that RMS error is only a secondary indicator of relative velocity model quality.

My method of using Pareto charts to calibrate joint optimization objective functions applies to many optimization problems beyond just geophysics. The technique that I described should be explored by anyone experiencing difficulty obtaining a convergent joint optimization. The logical next step would be to automate this process by examining how well the trend of the Pareto chart matches a linear fit. The way that I mapped the solidus and liquidus is a very straight-forward method to create the outline of a cooling schedule, particularly the initial and final temperatures. Here, I determined the critical temperature empirically by testing temperatures just above the solidus. While this proved effective, this is an area of ongoing research.

The improvements to seismic imaging demonstrated in this thesis can influence new development at San Emidio. U.S. Geothermal has the added ability to compare velocity model results with both the known stratigraphic section and proprietary well

data to tie lithologic contacts to reflectors. Furthermore, a more accurate velocity-to-density conversion can be calibrated by looking at velocity and density logs collected by Chevron in the 70's that I did not have access to; this relationship could also include an extra term to account for variation with depth. Using an empirical velocity-density relationship could reduce seismic-gravity data inconsistency and refine seismic imaging even further. Imaging may also be improved by using a more advanced migration algorithm, such as full waveform inversion. My results shed light on the lateral position of three faults, including one in the Mesozoic basement; that fault would be an ideal target according to Mayhew (2013). I showed that the valley is at least 1,500 m (4,900 ft) deep, which was not constrained in previous velocity models.

The joint optimization procedure can also positively impact geothermal exploration worldwide. This technique should be tried anywhere that difficult seismic imaging is encountered. First, velocity models should be converted to density models and gravity profiles computed; if these profiles match gravity already, joint optimization might not result in a different outcome. Second, directional gravity gradients must be examined to check if cylindrical symmetry is a valid assumption. The old strategy of forward-modeling density models to match gravity data could be replaced by my joint optimization technique, removing the need to purchase a separate gravity-modeling software package.

2.5 Conclusions

A stable, convergent joint seismic-gravity optimization algorithm has been presented. Seismic migrations that use velocity models produced by Plotrefa™ and SeisOpt® Pro™ have shallow velocity pull-ups; joint optimization resolves these shallow velocity artifacts. Synthetics demonstrate that joint optimization produces more accurate results than standalone seismic optimization. Jointly optimized velocity models are constrained below the deepest seismic raypath, which improves coherency of reflectors at depth. In this case, deeper velocity control reveals that the valley at San Emidio is deeper than 1,500 m (4,900 ft), which conflicts with the prior shallow valley interpre-

tation of Rhodes (2012). The migration using my jointly optimized velocity model shows evidence for the rangefront fault, which is partially observed in the migration using the SeisOpt® Pro™ velocity model, and absent in the migration that uses the Plotrefa™ velocity model. Joint optimization produces velocity models that are more accurate, but have higher RMS error. All velocity modeling techniques I used have similar efficiency and time costs.

Chapter 3 Future Work

Further testing is needed to validate the benefits of joint optimization shown in this thesis. Applying this technique to other seismic lines at San Emidio would be a good start, particularly with access to well logs. The methods outlined here can also be applied to other geothermal sites in the Great Basin that have long-offset seismic and gravity data, such as Astor Pass and Soda Lake. It would be interesting to optimize the entire 3D grid of gravity data and 10 lines of seismic data simultaneously; this could reveal bedrock morphology in three dimensions. Calibrating the velocity-to-density relationship with density and sonic (P-wave velocity) logs could help remove the inconsistencies that are resulting in higher RMS errors when joint optimization is used. Well logs could also be easily incorporated as a priori information into the simulated annealing algorithm as a form of Tikonov regularization in the objective function.

In this thesis, my standard acceptance criteria is met when seismic AND gravity RMS errors are reduced; this could be changed to accepting any model that expands the Pareto front. Optimizing this way would produce a suite of models ranging from the lowest gravity error to the lowest seismic error; this would reveal how adding gravity constrains the velocity model. It would be useful to explore what types of models joint optimization performs better on; for instance, I found that joint optimization performs poorly using synthetics with low-velocity zones. Quantifying the joint optimization sensitivity kernel would be good evidence that we are in fact constraining elements below the deepest raypath. Running multiple simulated annealing optimizations allowed the creation of stochastic velocity models with attached figures of element-wise variance; this showed that shallow regions are robust, while areas below the primary refractor were poorly constrained. This type of analysis could provide quantitative control on the location of the bedrock interface. It would be interesting to test genetic algorithms, particularly due to their compatibility with

parallel computing. With a supercomputer, the fitness landscape could be mapped fully, which would facilitate insights into the convergence process.

As opposed to the technique presented here, which only utilizes first arrival information, full waveform inversion (FWI) takes advantage of all the reflectors in the seismogram. Implementing FWI would help tune up velocity models at geothermal sites, particularly by fully modeling triplications. However, researchers must first figure out how to cope with the increased noise encountered in our dataset. One suggestion would be to first perform FWI on the long-wavelength features before scaling up to higher frequencies. I suspect that the cycle-skipping problem of FWI would make convergence very difficult, unless the starting model was very close to the answer. Solving the cycle-skipping problem of FWI and reducing the steep computational costs are currently areas of intensive ongoing research. Another route could be implementing reflector coherency into the objective function.

We showed how adding gravity to the optimization can improve velocity model accuracy at a geothermal site, but it remains to be seen what effects adding magnetic susceptibility or electrical resistivity into the optimization would do. Joint seismic-magnetic optimization has been shown to be very effective. Converting my gravity model into a magnetic model is as easy as converting density into magnetic susceptibility and changing the scaling factors. Joint seismic-electrical optimization could even take advantage of magneto-telluric and multichannel DC-resistivity datasets simultaneously.

If anyone is interested in utilizing the data, codes, and scripts described and used in this thesis, you can find them by contacting Dr. John Louie at louie@seismo.unr.edu or Kyle Basler-Reeder at metaheurist@gmail.com.

References

Abbott, R. E., Louie, J. N., Caskey, S. J., and Pullammanappallil, S. (2001). Geophysical confirmation of low-angle normal slip on the historically active Dixie Valley fault, Nevada. *Journal of Geophysical Research*, 106(B3):4169–4181.

Anderson, R. B. (2013). *Structural Controls of the Emerson Pass Geothermal System, Washoe County, Nevada*. Master's Thesis, University of Nevada - Reno. ProQuest. 202 pg. #1545675.

Basu, A. and Frazer, L. N. (1990). Rapid Determination of the Critical Temperature in Simulated Annealing Inversion. *Science*, 249(4975):1409–1412.

Beaty, K. S., Schmitt, D. R., and Sacchi, M. (2002). Simulated annealing inversion of multimode Rayleigh wave dispersion curves for geological structure. *Geophysical Journal International*, 151(2):622–631.

Berger, P., Got, J. L., González, C. V., and Monteiller, V. (2011). Seismic tomography at Popocatépetl volcano, Mexico. *Journal of Volcanology and Geothermal Research*, 200:234–244.

Biondi, B., Nichols, D., and Sava, P. (2014). Introduction to this special section: Imaging migration. *The Leading Edge*, 33(9):950–950.

Blackwell, D., Richards, M., Frone, Z., Ruzo, A., Dingwall, R., and Williams, M. (2011). Temperature-At-Depth Maps For the Conterminous US and Geothermal Resource Estimation. *GRC Transactions*, Vol 35:1545–1550.

Boulanger, O. and Chouteau, M. (2001). Constraints in 3D Gravity Inversion. *Geophysical Prospecting*, 49:265–280.

Brocher, T. M. (2005). Empirical relations between elastic wavespeeds and density in the Earth's crust. *Bulletin of the Seismological Society of America*, 95(6):2081–2092.

Brown, M. G. (1982). Application of the WKBJ Green's function to acoustic propagation in horizontally stratified oceans. *The Journal of the Acoustical Society of America*, 71(6):1427.

Cambois, G. (2000). Zero-phasing the zero-phase source. *The Leading Edge*, 19(1):72–75.

Černý, V. (1985). Thermodynamical approach to the traveling salesman problem: An efficient simulation algorithm. *Journal of optimization theory and applications*, 45(1):41–51.

Chávez-Pérez, S., Louie, J. N., and Pullammanappallil, S. K. (1998). Seismic depth imaging of normal faulting in the southern Death Valley basin. *Geophysics*, 63(1):223–230.

Christensen, N. I. and Mooney, W. D. (1995). Seismic velocity structure and composition of the continental crust: A global view. *Journal of Geophysical Research*, 100(B6):9761–9788.

Chunduru, R. K., Sen, M. K., and Stoffa, P. L. (1997). Hybrid optimization methods for geophysical inversion. *Geophysics*, 62(4):1196–1207.

Claerbout, J. F. (1985). *Imaging the Earth's Interior*. Wiley-Blackwell. 398 pg.

Claerbout, J. F. (1997). Introduction to Kirchhoff migration programs. *Stanford Exploration Project*, 73:385–391.

Colwell, C., VanWijk, K., Liberty, L., Warren, I., and Revil, A. (2012). Integrated geophysical exploration of a known geothermal resource: Neal Hot Springs. In *SEG Technical Program Expanded Abstracts 2012*, pages 1–5. Society of Exploration Geophysicists.

Constable, C. G., Parker, R. L., and Constable, S. C. (1987). Occam's Inversion: A Practical Algorithm for Generating Smooth Models from Electromagnetic Sounding Data. *Geophysics*, 52(3):289–300.

Coolbaugh, M. F., Raines, G. L., and Zehner, R. E. (2006). Prediction and discovery of new geothermal resources in the Great Basin: Multiple evidence of a large undiscovered resource base. *PROCEEDINGS, Twenty-First Workshop on Geothermal Reservoir Engineering*, 30:867–874.

Cumming, W. B. (2009). Geothermal resource conceptual models using surface exploration data: Proceedings of the 34th Workshop on Geothermal Reservoir Engineering.

Delwiche, B. (2007). *Oligocene paleotopography and structural evolution of the Pah Rah Range, western Nevada: Implications for constraining slip on the right-lateral Warm Springs Valley fault in the northern Walker Lane*. Master's Thesis, University of Nevada - Reno. ProQuest. 139 pg. #1446438.

Dering, G. (2013). *Structural Controls of the Tuscarora Geothermal Field, Elko County, Nevada*. Master's Thesis, University of Nevada - Reno. ProQuest. 91 pg. #1540175.

Drakos, P. S. (2007). *Tertiary Stratigraphy and Structure of the Southern Lake Range Northwest Nevada: Assessment of Kinematic Links Between Strike-slip and Normal Faults in the Northern Walker Lane*. Master's Thesis, University of Nevada - Reno. ProQuest. 165 pg. #1442868.

Eneva, M., Falorni, G., Teplow, W., and Morgan, J. (2011). Surface deformation at the San Emidio geothermal field, Nevada, from satellite radar interferometry. *PROCEEDINGS, Twenty-First Workshop on Geothermal Reservoir Engineering*, 35:1647–1653.

Faulds, J., Coolbaugh, M., and Bouchot, V. (2010). Characterizing structural controls of geothermal reservoirs in the Great Basin, USA, and Western Turkey: Developing Successful Exploration Strategies in Extended Terranes. *Proceedings World Geothermal Congress*, pages 1–11.

Faulds, J. E., Coolbaugh, M. F., and Vice, G. S. (2006). Characterizing structural controls of geothermal fields in the northwestern Great Basin: A progress report. *GRC Transactions*, 30:69–76.

Faulds, J. E., Hinz, N. H., Kreemer, C., and Coolbaugh, M. F. (2012). Regional Patterns of Geothermal Activity in the Great Basin Region, Western USA: Correlation With Strain Rates. *GRC Transactions*, 36:1–6.

Fedi, M., Florio, G., and Rapolla, A. (1998). 2.5D modelling of Somma–Vesuvius structure by aeromagnetic data. *Journal of Volcanology and Geothermal Research*, 82:239–247.

Gardner, G., Gardner, L. W., and Gregory, A. R. (1974). Formation velocity and density-the diagnostic basics for stratigraphic traps. *Geophysics*, 39(6):770–780.

Geometrics (2009). *SeisImager2D Manual v. 3.3*. 257 pg.

Godfrey, N. J., Beaudoin, B. C., Klemperer, S. L., and Group, M. W. (1997). Ophiolitic basement to the Great Valley forearc basin, California, from seismic and gravity data: Implications for crustal growth at the North American continental margin. *Geological Society of America Bulletin*, 109(12):1536–1562.

Haber, E. and Holtzman Gazit, M. (2013). Model Fusion and Joint Inversion. *Surveys in Geophysics*, 34(5):675–695.

Hale, D. and Claerbout, J. F. (1983). Butterworth dip filters. *Geophysics*, 48(8):1033–1038.

Harris, B. (2012). Geophysical technologies for geothermal well field development in sedimentary basins. *ASEG Extended Abstracts*, 2012(1):1–3.

Honjas, W. and Pullammanappallil, S. K. (1997). Predicting shallow Earth structure within the Dixie Valley geothermal field, Dixie Valley, Nevada, using a nonlinear velocity optimization scheme. *PROCEEDINGS, Twenty-First Workshop on Geothermal Reservoir Engineering*, pages 153–160.

Hubbert, M. K. (1948). A line-integral method of computing the gravimetric effects of two-dimensional masses. *Geophysics*, 13(2):215–225.

Ingber, L. (1993). Simulated annealing: Practice versus theory. *Mathematical and computer modelling*, 18:29–57.

Jolie, E., Moeck, I., and Faulds, J. E. (2015). Quantitative structural–geological exploration of fault-controlled geothermal systems—A case study from the Basin-and-Range Province, Nevada (USA). *Geothermics*, 54:54–67.

Kent, T. (2013). *Comparing Deformation at Soda Lake Geothermal Field from GPS and 3D Seismic*. Master's Thesis, University of Nevada - Reno. ProQuest. 41 pg. #1540191.

Kirkpatrick, S., Gellat Jr, C. D., and Vecchi, M. P. (1983). Optimization by simulated annealing. *Science*, 220:671–680.

Lee, C.-Y. and Lee, D. (2013). Determination of initial temperature in fast simulated annealing. *Computational Optimization and Applications*, 58(2):503–522.

Lelièvre, P. G., Farquharson, C. G., and Hurich, C. A. (2012). Joint inversion of seismic traveltimes and gravity data on unstructured grids with application to mineral exploration. *Geophysics*, 77(1):K1–K15.

Louie, J. N., Clayton, R. W., and LeBras, R. J. (1988). Three-dimensional imaging of steeply dipping structure near the San Andreas fault, Parkfield, California. *Geophysics*, 53:176–185.

Louie, J. N., Pullammanappallil, S. K., and Honjas, W. (2012). Advanced seismic imaging for geothermal development. In *SEG Technical Program Expanded Abstracts 2012*, pages 1–6. Society of Exploration Geophysicists.

Louie, J. N. and Qin, J. (1991). Subsurface imaging of the Garlock Fault, Cantil Valley, California. *Journal of Geophysical Research*, 96(B9):14461–14479.

Ludwig, W. J., Nafe, J. E., and Drake, C. L. (1970). *Ideas and Observations on Progress in the Study of the Seas*, volume 4 of *Seismic Refraction*. Wiley-Interscience, New York.

Lumley, D. E., Claerbout, J. F., and Bevc, D. (2012). Anti-aliased kirchhoff 3-D migration. In *SEG Technical Program Expanded Abstracts 1994*, pages 1282–1285. Society of Exploration Geophysicists.

Luo, S. and Hale, D. (2014). Least-squares migration in the presence of velocity errors. *Geophysics*, 79:S153–S161.

Mankhemthong, N. (2008). *Structure of the Inter-basin Transition Zone Between Dixie Valley and Fairview Valley, Nevada, USA*. Master's Thesis, University of Nevada - Reno. ProQuest. 132 pg. #1460765.

Matek, B. (2014). 2014 Annual U.S. & Global Geothermal Power Production Report. pages 1–25.

Matlick, S. (1995). *San Emidio Geothermal System*. Empire, Nevada. October 1995 GRC Field Trip Report. 18 pg.

Mayhew, B. A. (2013). *A 3D Characterization of the Astor Pass Geothermal System, Washoe County, Nevada*. Master's Thesis, University of Nevada - Reno. ProQuest. 111 pg. #1545707.

Metropolis, N., Rosenbluth, A. W., Rosenbluth, M. N., Teller, A. H., and Teller, E. (1953). Equation of State Calculations by Fast Computing Machines. *The Journal of Chemical Physics*, 21(6):1087.

O'Donnell Jr, T. M., Miller, K. C., and Witcher, J. C. (2001). A seismic and gravity study of the McGregor geothermal system, southern New Mexico. *Geophysics*, 66(4):1002–1014.

Pullammanappallil, S. K. (1994). *Nonlinear Optimization to Estimate Velocities and Image Reflectors from Multi-offset Seismic Data*. PhD Dissertation, University of Nevada - Reno. Proquest. 274 pg. #9524649.

Reeder, K., Louie, J. N., Kent, G., and Pullammanappallil, S. K. (2014). Efficient 2D finite element gravity modeling using convolution. *SEG Technical Program Expanded Abstracts 2014*, pages 1254–1258.

Rhodes, G. T. (2012). *Structural Controls of the San Emidio Geothermal System, Northwestern Nevada*. Master's Thesis, University of Nevada - Reno. ProQuest. 81 pg. #1505172.

Robinson, E. A. (1986). Migration of seismic data by the WKBJ method. *Proceedings of the IEEE*, 74(3):428–439.

Rovetta, D., Colombo, D., Curiel, E. S., and Ley, R. E. (2013). 3D Seismic-gravity Simultaneous Joint Inversion for Near Surface Velocity Estimation. *75th EAGE Conference & Exhibition incorporating SPE EUROPEC*, pages 1–6.

Roy, L., Sen, M. K., McIntosh, K., Stoffa, P. L., and Nakamura, Y. (2005). Joint inversion of first arrival seismic travel-time and gravity data. *Journal of Geophysics and Engineering*, 2(3):277–289.

Sen, M. K. and Stoffa, P. L. (2013). *Global Optimization Methods in Geophysical Inversion*. Cambridge University Press. 304 pg.

Snieder, R. and Trampert, J. (2000). Linear and Nonlinear Inverse Problems. In *Geomatic Method for the Analysis of Data in the Earth Sciences*, pages 93–164. Springer Berlin Heidelberg, Berlin, Heidelberg.

Suman, B. and Kumar, P. (2005). A survey of simulated annealing as a tool for single and multiobjective optimization. *Journal of the Operational Research Society*, 57(10):1143–1160.

Szu, H. and Hartley, R. (1987). Fast simulated annealing. *Physics letters A*, 122:157–162.

Talwani, M., Worzel, J. L., and Landisman, M. (1959). Rapid Gravity Computations for Two-Dimensional Bodies with Application to the Mendocino Submarine Fracture Zone. *Journal of Geophysical Research*, 64:49–59.

Telford, W. M. and Sheriff, R. E. (1990). *Applied Geophysics*. Cambridge University Press. 770 pg.

Teplow, W., Faulds, J., Rhodes, G., Moeck, I., Eneva, M., and Pullamannapallil, S. (2011). Finding Large Aperture Fractures in Geothermal Resource Areas Using a Three-Component Long-Offset Surface Seismic Survey, PSInSAR, and Kinematic Structural Analysis. DOE Award No.: DE-EE0002847. *US Geothermal, Inc.*, pages 1–20.

Teranishi, Y., Mikada, H., Goto, T.-n., and Takekawa, J. (2012). Three-dimensional joint inversion of gravity and magnetic anomalies based on density-magnetization relationship. In *SEG Technical Program Expanded Abstracts 2012*, pages 1–5. Society of Exploration Geophysicists.

Thorson, J. R. and Claerbout, J. F. (1984). Velocity stack and slant stack inversion methods. *Geophysics*, 50(12):2727–2741.

Tieman, H. J. (1995). Migration velocity analysis: Accounting for the effects of lateral velocity variations. *Geophysics*, 60(1):164–175.

Van Avendonk, H. J. A., Harding, A. J., Orcutt, J. A., and McClain, J. S. (2001). Contrast in crustal structure across the Clipperton transform fault from travel time tomography. *Journal of Geophysical Research*, 106(B6):10961–10981.

Vasco, D. W., Peterson Jr, J. E., and Majer, E. L. (1996). Nonuniqueness in traveltime tomography: Ensemble inference and cluster analysis. *Geophysics*, 61(4):1209–1227.

Vermeesch, P. M., Morgan, J. V., and Christeson, G. L. (2009). Three-dimensional joint inversion of traveltime and gravity data across the Chicxulub impact crater. *Journal of Geophysical Research*, 114:2–19.

Vice, G. S. (2008). *Structural Controls of the Astor Pass-Terraced Hills Geothermal System in a Region of Strain Transfer in the Western Great Basin, Northwestern Nevada*. Master's Thesis, University of Nevada - Reno. ProQuest. 128 pg. #1456425.

Vidale, J. (1988). Finite-difference calculation of travel times. *Bulletin of the Seismological Society of America*, 78(6):2062–2076.

Xiao, C., Peng, Y., Lei, Z. L., Yang, X., and Lin, W. J. (2011). Applying improved very fast simulated annealing in regularized geophysical joint inversion. *2011 Seventh International Conference on Natural Computation (ICNC)*, 4:1998–2001.

Yang, H., Wang, J. L., Wu, J. S., Yu, P., and Wang, X. M. (2002). Constrained Joint Inversion of Magneto-telluric and Seismic Data Using Simulated Annealing Algorithm. *Chinese Journal of Geophysics*, 45(5):764–776.

Zhang, L. B., Yao, Z. X., Ji, C., and Zhang, Z. J. (1997). Fast simulated annealing and its application. *Oil Geophysical Prospecting in Chinese*, 32:654–660.